3-D MORPHOMETRY AND NON-RIGID REGISTRATION FOR QUANTITATIVE ANALYSIS AND CLINICAL ASSESSMENT IN RADIOLOGY

BY GABRIELA NICULESCU

A dissertation submitted to the

Graduate School—New Brunswick

Rutgers, The State University of New Jersey

and

The Graduate School of Biomedical Sciences

University of Medicine and Dentistry of New Jersey

in partial fulfillment of the requirements for the

Joint Degree of Doctor of Philosophy

Graduate Program in Biomedical Engineering

Written under the direction of

Professor David J. Foran

and approved by

_____

_____

_____

_____

New Brunswick, New Jersey

May, 2008

ABSTRACT OF THE DISSERTATION

3-D Morphometry and Non-rigid Registration for Quantitative Analysis and Clinical Assessment in Radiology

by Gabriela Niculescu

Dissertation Director: Professor David J. Foran

The capacity to reliably track, model and characterize morphometric changes in anatomic structures and tumors from 3-D images sequences is extremely valuable in staging disease progression and assessing response to treatment.

We have designed, developed and evaluated two approaches to facilitate clinical assessment in diagnostic radiology. The first is a tool for performing comparative morphologic analysis and the second is a registration strategy which can compensate for changes in shape that occur in deformable organs when assessing response to treatment across consecutive imaging studies. The first prototype system was used to characterize the morphology of ventricles from MR brain scans of patients who had been diagnosed with Bipolar Disorder or Asperger's Syndrome. Preliminary studies demonstrated that conventional volumetric measurements were insufficient for detecting and characterizing subtle changes in anatomic profiles. We have investigated the use of a double elliptic Fourier transform to discriminate among 3-D changes of anatomic structures. It was shown that characterization using low frequency elliptic Fourier descriptors prov ided an accurate representation of the anatomical structures while allowing for reliable group separation. The shape-based 3-D object representation of brain structures developed

in this project may provide insight regarding the underlying mechanisms leading to the onset and progression of these disorders.

As an extension of these studies, a deformable registration technique was evaluated for tracking tumor response to radiofrequency ablation of patients with liver malignancies. The method exploits the combined power of global and local alignment of pre- and post-treatment CT images. The distinguishing characteristics of the system is that it can infer volumetric deformation based upon surface displacements using a linearly elastic finite element model (FEM). Using both 2-D synthetic phantoms and 3-D beef liver data we performed the simulation of gold standard registration by measuring the accuracy of non-rigid deformation. The voxel mean displacement error of deformation demonstrates that the technique provides valuable information for surgical interventions. This approach is general methodology for tracking deformable organs using non-rigid registration with respect to FEM simulations. It provides a basis for monitoring tissue response and therapy planning for a range of medical applications in the brain, breast or heart.

Acknowledgements

I would like to express my great thanks and appreciations to my advisor Dr. David J. Foran for his encouragement and patience during the course of this research. His insight and support are deeply appreciated.

I am deeply indebted to Dr. John L. Nosher for embarking with me on this thesis journey. I could not have wished for better collaborator and coache. Your contributions, detailed comments and insight have been of great value to me.

Partial portions of this dissertation was published in:

Gabriela Niculescu, Louay Toni, David J. Foran, John L. Nosher, Kevin DeMarco, "Dynamic Imaging Database for 3D Morphologic Analysis and Clinical Assessment in Diagnostic Radiology", American Medical Informatics Association (AMIA), San Antonio, TX, 2002.

Gabriela Niculescu, David J. Foran, John L. Nosher, " Non-rigid Registration of the Liver in Consecutive CT Studies for Assessment of Tumor Response to Radiofrequency Ablation", 29th Annual International Conference of the IEEE Engineering in Medical and Biology Society (EMBC), Lyon, France, 2007.

Dedication

To my family.

Table of Contents

List of Tables

List of Figures

Chapter 1

Introduction

Modern imaging techniques have become invaluable clinical and research tools for visualizing anatomic structures, non-invasively, however, some of the technical challenges which arise during post-acquisitional image analysis cause investigators to opt for semi-quantitative studies and/or subjective interpretations of data. With the increased use of 3-D imaging methods such as computed tomography (CT), magnetic resonance (MR) imaging and ultrasonography (US) being used for diagnosis, therapy and surgical planning the need for improved methods for image analysis has become apparent. The development of more reliable methods for shape analysis and registration could lead to further insight as to the underlying biological mechanisms and pathological processes of disease onset and progression.

1.1 Problems Encountered in Neuroimaging

In neuroimaging applications volumetric measurements are one of the most frequently utilized quantitative measurements used in assessing brain structures. Enlarged ventricular size has been cited as an important criteria for characterizing Bipolar disorder and Asperger's syndrome [1, 2].

Asperger's syndrome is a pervasive developmental disorder characterized by major difficulties in social interaction and unusual patterns of interest and behavior. Its heritability remains questionable. Clinical features of the syndrome include diminished expression of empathy, poor communication capacity, monotonic speech, diminished motor coordination, intense absorption of seemingly unusual information and a seemingly diminished ability to develop social skills [3].

Bipolar disorder is a major affective disorder characterized by a disorganization of

Table 1.1: Volumetric measurements for LV - left ventricle RV- right ventricle

	LV	RV	Total ventricles
Controls			
Mean	6380.47	5983.79	12364.26
St. Dev.	2306.71	2138.67	4377.27
Asperger's Syndrome			
Mean	7891.46	7515.57	15407.03
St. Dev.	3627.50	4344.30	7481.45
Bipolar Disorder			
Mean	7802.71	7340.11	15142.82
St. Dev.	2745.43	4125.49	6288.81

feelings. The key identifying feature of Bipolar disorder is the alternation of maniac episodes with major depressive episodes in an unending roller coaster ride from the peaks of elation to the depths of despair [4]. Periods of depression are characterized by torpid speech and movement, loss of appetite and disturbed sleeping patterns. Episodes of mania are characterized by an unaccountable euphoria, delusions of grandeur and excessive speech and motor activity. Average onset of the disease is around the age of 21 years with similar rates in males and females throughout the world [5]. Bipolar disorder is associated with a high level of morbidity, and it has been estimated that approximately 15% of patients eventually die by suicide [6].

The standard method for evaluating imaging studies of those patients involves systematic slice-by-slice interactive processing of volumetric data. During feasibility experiments Analyze AVW software (Mayo Clinic) was used to interactively segment and analyze MR image data sets. Forty MRI brain scans were acquired using a 1.5Tesla GE Sigma scanner located at the Laurie Imaging Center (UMDNJ-RWJMS). The study consisted of fourteen patients who had been diagnosed with Bipolar disorder, seventeen who had been diagnosed with Asperger's Syndrome and nine patients served as controls. Patients ranged from 7 to 14 years of age and were predominantly male. Table 1 shows the ventricular volumes that were computed during preliminary studies.

Although the numerical difference between the mean total ventricular volume for the control group and either disorder would seem sufficient to distinguish between "normal" and "abnormal" ventricles (3042.77 mm3 control - Asperger's Syndrome, and 2778.56

mm3 control - Bipolar disorder), the large standard deviation for each group in this study strongly suggested that volumetric measurements alone were insufficient for detecting abnormalities. The low discriminatory power may be attributed, in part, to the fact that shape differences among the structures are not adequately captured through the volumetric characterization of the morphology. Our preliminary studies indicate that local or global parameters may serve to improve accuracy of classifications.

1.2 Problems Encountered in Liver Therapy Imaging

Hepatocellular carcinoma (HCC) is the common primary malignant tumor of the liver. Although resection or liver transplantation are considered potentially curative or survival enhancing treatment options, only 20%-30% of patients with HCC are candidates for intervention [7]. Several minimally invasive imaging-guided ablative therapies using thermal energy sources such as lasers, microwaves, radioflequency (RF) and high intensity focused ultrasound (HIFU) are rapidly developing alternatives to surgical treatment in primary liver malignancies [8, 9]. Possible advantages of ablative therapies over open surgery include excellent local control with less recovery times at a reasonable cost, with low morbidity and mortality rates. The main goal of thermal ablation therapy is to destroy an entire tumor by using heat to kill the malignant cells without damaging adjacent vital structures. For most thermal ablation methods, energy is applied percunaneously by using a needle-shaped applicators. Goldberg et al [10] described the basic relationship guiding thermal ablation induced coagulation necrosis as follows:

$$coagulation\,necrosis = energy\,deposited * local\,tissue\,interactions - heat\,loss$$

The ability to produce a tumor necrosis is dependent on local physiologic tissue characteristics and several technology-based factors given the multiple energy sources to achieve thermal ablation, the different strategies for applying them and the different probe devices including hooked electrodes or internally cooled single or triple electrodes.

Per cutaneous radiofrequency ablation (RFA) is the method receiving the greatest clinical attention to date, which has proved very effective and safe in treating patients with unresectionable hepatic tumors. Patients with HCC are particularly well-suited for

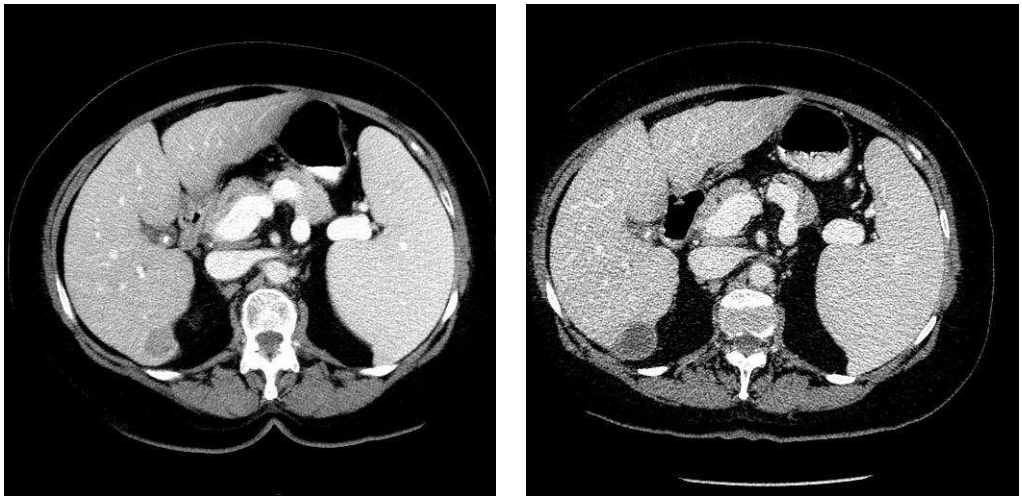

Figure 1.1: Pre and post RFA treatment CT images

primary treatment with radiofrequency ablation (RFA) given the high rates of multiple tumor appearance over time, concurrent hepatitis infection and liver cirrhosis. Multiple clinical studies have been performed to evaluate the use of RFA in the treatment of HCC [11, 12, 13, 14]. Results of early clinical trials showed a complete tumor necrosis in 83% of tumors less than 3cm in patients with HCC who underwent RFA [15].

Liver tumor ablation carried out by heating the tumor using radiofrequency (RF) energy which is delivered through an electrode which is actually, a thin needle that is electrically insulated along all but the distal 1-3 cm of the shaft. Connected to the RF generator, the uninsulated distal portion of the probe tip emanates current waves. Heat is produced by ionic agitation surrounding the electrode as the current flows to the ground resulting in coagulation necrosis. When mono polar RF generator is used the ground is a usually a foil pad placed on the patientś back, whereas in the bipolar system, a second electrode is used as ground. The deposition of the energy in the tissue generates a dark thermal lesion often surrounded by a bright edematous rim. The RFA procedure is considered technically successful if the tumor and a safety margin of 5-10 mm of normal hepatic tissue are completely included in the ablation zone [16] as shown in the Figure 1.1.

Localization of tumors using CT imaging-guided techniques and pre- and post-procedural analysis to ensure the accuracy of ablative margins are both extremely challenging due to the following problems:

- The liver is a highly deformable soft tissue organ. A significant amount of non-linear motion or deformation occurs in the liver in response to differences in the positioning of patients undergoing consecutive imaging studies. Deformation also arises due to respiratory motion, and surgical manipulations.

- The shape and the size of the tumor appearance depends on the dynamics of the contrast-enhancing agent used in CT images. Typically, standard CT images without contrast are obtained to plan the procedure and to guide the ablation applicator placement. Contrast agents may be administrated only once during the procedure and the intensity of the image vary considerably between the arterial and the portal phases of the CT image protocol. The majority of liver tumors may appear clear only in the two minutes following the contrast agent injection. The apparent boundaries of the tumor often change dramatically during the course of this time.

- Furthermore, real-time imaging can not be maintained throughout the entire RFA procedure. The intervention radiologist visually consults the pre-procedure image studies during the course of the RFA procedure in an attempt to locate the center of the same tumor. Because there is no way to compress the region of the liver where the tumor is located when the tip of the needle reaches the interface between two different types of tissue, further insertion tends to push the tissue rather than piercing it, which gives rise to unwanted deformations.

All the above limitations make the RFA procedure very sensitive to the initial placement of the needle. It would be very useful to develop techniques to help the interventional radiologist in predicting tumor displacement, thereby allowing accurate tracking of lesion across consecutive studies. To determine the success of the treatment one can register and compare imaged tumor characteristics before and after treatment.

1.3 Specific Aims

In the neuroimaging study we investigated the use of a double elliptic Fourier transform to discriminate among 3-D changes of anatomic structures in MR brain scans. Through a series of experiments it was shown that shape characterization using low frequency elliptic Fourier descriptors (EFD) provided an accurate representation of anatomical structures. Whereas volumetric measurements did not provide the means for discriminating between diseases and control groups. Furthermore, our experiments showed that 3-D shape signatures based upon a double EFD algorithm did provide accurate group separation among disorders and normals.

In the liver imaging study we presented a surface based non-rigid method for tracking tumor across pre- and post-treatment CT liver images using a finite element model based deformable system. The strategy of the algorithm is twofold: the first step is to align the mesh surfaces, using a modified Iterative Closest Point (ICP) algorithm that determine the proper correspondence of the boundary points to drive the transformation. The second step is to model the volumetric deformation using a linearly elastic finite element model (FEM) that has boundary conditions generated from the registered data. Using both 2D synthetic phantom and real 3D beef liver data we introduced a set of gold standard deformations to measure the accuracy of the newly developed non-rigid registration.

1.4 Thesis Outline

Chapter II present the neuroimaging study:

Section I presents the background of shape analysis relevant to our work in neuroimaging - the theory behind the boundary encoding.

Section II presents an overview of elliptic Fourier descriptors for 2-D boundaries.

Section III presents the encoding algorithm for 3-D Fourier descriptors. We describe the approach for registering two data sets using the Iterative Closest Point (ICP) algorithm and the object classification method is evaluated for performance.

Section IV presents the results obtained after applying 3-D Fourier encoding algorithm for the surface reconstruction. Some data compression, area and volume issues are also addressed. Results from registration and re-section algorithms are presented and the image database design is described.

Section V draws the conclusions for the neuroimaging study and gives the perspective of future research.

Chapter III presents liver therapy study:

Section I presents the liver registration study starting with related work.

Section II presents three algorithms for finding the correspondence of two data sets: Curvature Scale Space (CSS), a modified Iterative Closest Point (ICP) algorithm, and Robust Point Matching (RPM).

Section III presents a briefly introduction in the theory behind Finite Element Method (FEM).

Section IV presents the tumor tracking model based on the combination of registration and linearly elastic finite element analysis.

Section V presents a 2D rubber phantom and a 3D real beef liver studies used to validate the performance of our model simulation for predicting the tumor displacement. We track the position of several markers before and after different deformations.

Section VI presents a clinical study involving three different patients with hepatocellular carcinomas. The lesion's displacement is tracked for each patient.

Section VII draws the conclusions for the liver therapy study and gives the perspective of future research.

Chapter 2

Neuroimaging Study

2.1 Related Work for Shape Analysis

The overall goal of shape analysis research is to provide a reliable means for comparing arbitrary shapes in two or more dimensions. Shape is one of important features for describing and representing an object. Even though it is conceptually easy to understand the notion of 2-D shape, it can sometimes be difficult to represent, describe and define. Shape representation methods result in a non-numeric (e.g. graph or an image) representation whereas shape description methods result in numerical descriptors which follow the shape representation [17]. For many medical imaging applications some of the most desirable properties of the shape descriptor vector also called the feature vector is that it be invariant to scale, translation, and rotation while simultaneously capturing the essence the shape.

Shape analysis algorithms can be classified according to a variety of criteria. Pavlidis [18] proposed the following classification scheme. The first is based on shape boundary points alone, rather than on interior shape descriptions which are considered as global algorithms. The second scheme called shape analysis algorithms are based on either numeric results, in which case there is a scalar transform, or non-numeric results which pertain to space domain techniques. For example the chain code described in [19, 20] is considered a space domain technique because it transforms one shape into another rather than into an array of scalar features. The third classification scheme is based on information preservation and information non-preserving methods which depends on whether shape reconstruction is possible from constituent descriptors or not. Non-preserving techniques are described in terms of very local characteristics such as symmetry, elongation and angularity. An example of an information non-preserving

method is the ratio of the square of the perimeter to the area [18].

In order to analyze and manipulate arbitrarily shaped objects which are embedded in 3-D image stacks a reliable, non-ambiguous means for describing those shapes is needed. It is often desirable to convert the arbitrary shape into a representative form that can be efficiently processed in terms of both computational time and memory space requirements. For such applications boundary representation is one of the most popular strategies. The boundary for any given imaged object can be considered a closed sequence of successive boundary pixels coordinates. If one needs to transmit an accurate description of the contour of a delineated tumor over a network, for example, the contour must first be represented (encoded) in a fashion which permits a reliable decoding and pictorial reconstruction at the receiving end.

The following subsections will provide an overview of the chain code and scalar Fourier transform methods respectively, which were used in preliminary feasibility experiments for boundary representation and boundary description.

2.1.1 Chain code - Boundary Space Domain Method

The process of adopting a symbolic convention and quantitatively identifying the description proprieties of the approach in terms of the convention is referred to as encoding. The following properties are desirable for any encoding scheme [19] :

1. the encoding scheme for arbitrary geometric curves should be simple, highly standardized and universally applicable to all continuous curves.

2. the encoding scheme must faithfully preserve the information of interest.

3. the encoding scheme should facilitate digital computer analysis of a given curve's properties.

The method for coding line drawings called chain code was introduced in 1961 by Herbert Freeman [19]. Chain codes are used to represent boundaries using a connected sequence of straight line segments of specified direction and length. Line structures are generated through quantization of tracings with a grid-intersection scheme, thus a boundary point

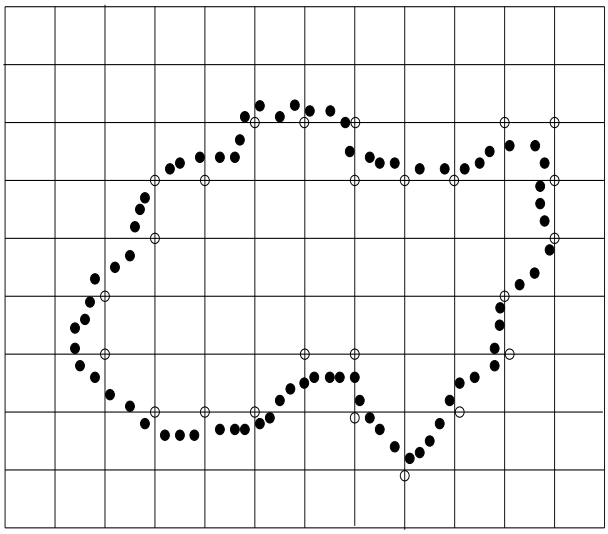

Figure 2.1: Result of boundary re-sampling with superimposed grid

is assigned to each node of the grid, depending on the proximity of the original boundary to a given node as shown in Figure 2.1.

On the digital (rectangular) grid, encoding is based on the fact that successive contour points are adjacent to one another. Freeman [19, 20] showed that if the 8-connected grid is employed, the chain code is defined as the digits from 0 to 7, assigned to the 8 neighboring grid points in a counter-clockwise sense. Since the accuracy of the resulting code representation depends on the spacing of the sampling grid, several different digitization methods have been suggested [21, 22].

A direct straight-line segment connecting two adjacent grid points is called a link. A continuous contour can be approximated by a sequence of links a_i. A link corresponds to one of eight standardized straight -line segments oriented in the direction $(\pi/4)a_i$, as measured counter-clockwise from the X axis of an Cartesian coordinate system. Each being length 1 or $\sqrt{2}$ depending, respectively, on whether a_i is even or odd. A chain is an ordered sequence of links written in the form:

$$C = a_1 a_2 ... a_n$$

An example of chain code $C = 00106001066565532454432 12$ is shown in Figure 2.2

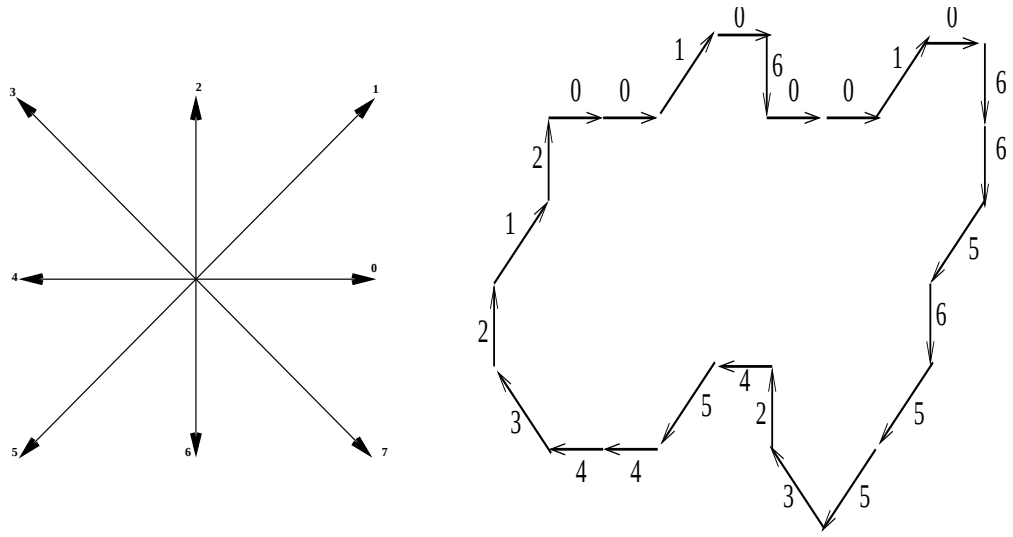

Figure 2.2: (a) Definition of the chain code 8 - connected (b) Chain code of the curve from Figure 1.1

The flexibility of the chain code representation is illustrated by the ease with which the inverse, length, width and height of the chain can be computed. The integral of a function with respect to the x axis, the first and second moments about x and y axis, and the distance between two connected points are also relatively simple operations [20]. The chain coding scheme can be easily extended to 3-D line structures quantized on a cubic lattice by assigning a symbol for each of the 26 possible directions [20]. The derivative chain code method given rise to numerous research activities implemented using a variety of algorithmic approaches [23, 24, 25, 26].

2.1.2 Fourier - Boundary Scalar Transform Method

The Fourier transform represents an orthonormal periodic signal which can be expressed as a weighted sum of known functions. An orthonormal set is desirable because it makes the parameters distinct and facilitates coefficient determination by avoiding redundancy. A general way, to decompose a function $X(t)$ on the interval $[a, b]$ is :

$$\phi(t) : X(t) = \sum_{n=1}^{\infty} C_n \phi(t) \qquad C_n = \int_a^b X(t)\phi_n(t)dt$$

where the coefficients C_n are the orthogonal projections of $X(t)$ onto the subspace generated by the n basis functions. In practice the degree of the sum is restricted and

the choice of its value is a trade off between desired accuracy and degree of smoothing. The usual basis functions are the sinusoids [18] which have the advantage of providing a notion of frequency.

Suppose that the boundary of a shape has N pixels numbered from 0 to $N-1$. The k-th pixel along the boundary has position (x_k, y_k) and we can describe the contour as two parametric equations:

$$x(k) = x_k$$

$$y(k) = y_k$$

The contour itself is periodic, therefore, it is possible to take the Fourier transform of each function and obtain two frequency spectra called Fourier descriptors (FD):

$$a_x(\nu) = F(x(k))$$

$$a_y(\nu) = F(y(k))$$

The major advantage of this method is that it is fairly straight forward to make slight modifications to the FD so that it becomes invariant to scale, translation, rotation and starting point of the contour .

The boundary scalar transform algorithms describe shape indirectly by means of a 1-D function which in turn can be used to characterize the shape of 2-D boundary. There are many different methods for 1-D boundary function representation and in this section we present some of different possible representations based on Fourier's parametrization that have been reported in the literature.

The tangent angle $\theta(l)$ versus arc length function is the 1-D boundary representation which was developed by Zahn and Roskies [27]. In this formulation if $\theta(l)$ is the angular direction of a clockwise oriented close curve at point l then the cumulative angular function $\phi(l)$ is defined as the net amount of angular bend between starting point $l = 0$ and point l. So $\phi(l) = \theta(l) - \theta(0)$, except for a possible multiple of 2π, where $\theta(0)$ is the absolute angular direction at the starting point as shown in the Figure 2.3.

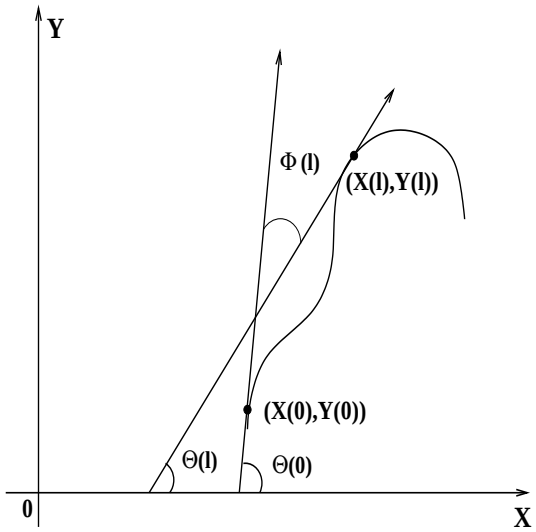

Figure 2.3: Parametric representation of a curve with tangential direction $\theta(l)$ and cumulative angular function $\phi(l)$

The domain of definition of function $\phi(l)$ is $[0, L]$, where L is the perimeter of close curve, then the function can be normalized and made dependent upon parameter $t \in [0, 2\pi]$. Letting $\phi^*(t)$ be the normalized variant $\phi^*(0) = \phi^*(2\pi) = 0$:

$$\phi^*(t) = \phi(\tfrac{Lt}{2\pi}) + t$$

Note that $\phi^*(t) \equiv 0$ for a circle, we map all the plane closed curves into the class of periodic functions on $[0, 2\pi]$ in such a way that all curves of identical shape and starting point become part of the same function ϕ^*[27]. The boundary function $\phi^*(t)$ is expanded as a Fourier series as:

$$\phi^*(t) = \mu_0 + \sum_{k=1}^{\infty}(a_k cos kt + b_k sin kt)$$

If (A_k, α_k) are the polar coordinates of (a_k, b_k) then the $\phi^*(t)$ expansion is given by:

$$\phi^*(t) = \mu_0 + \sum_{k=1}^{\infty} A_k cos(kt - \alpha_k)$$

The coefficients $\{\mu_0, a_k, b_k\}$ or $\{A_k, \alpha_k\}; k = 1..\infty$ are the k -harmonic Fourier descriptors (FD) which are used for shape characterization of the curve.

The tangent angle function also called the turning function has been used by Akin and his colleagues [28] to reliably represent and compare polygonal shapes. The function $\theta_A(s)$ measures the angle of the counter-clockwise tangent as a function of arc length s, which is measured from any given reference start point on the polygon's boundary. $\theta_A(s)$ becomes a function defined on $[0, 1]$ interval, assuming that all polygons are normalized so that their perimeter length is 1. Even though the turning angle method is invariant to scale and translation and can easily be made rotation invariant a drawback of this representation it is sensitive to small variations in shape.

Granlund [29], Richard and Hemani [30], and Persoon and Fu [31] presented the 1-D complex function of the form $z(l) = x(l) + jy(l)$ where l is the arc length parameter. In this formulation any point moving along the boundary generates a periodic complex function $z(l)$, which implies $z(l + nL) = z(l)$. Therefore the Fourier series expansion of $z(l)$ becomes:

$$z(l) = \sum_{-\infty}^{\infty} a_n e^{j2\pi nl/L}$$

where $z(l)$ is often referred to as a shape signature. The normalized Fourier coefficients are the Fourier descriptors :

$$a_n = \frac{1}{L} \int_0^L z(l) e^{-j2\pi nl/L} dl$$

One advantage of using the coordinates $z(l)$ instead of tangent angle $\theta(l)$ representation of the boundary curve is that the complex coordinates function is less sensitive to the inherent noise contained within fuzzy boundaries. The tangent angle function is related to the derivative of the coordinate function, thus small variations in the coordinate values of the boundary points can give rise to large variations in the direction of the tangent vector.

If $z^{(0)}(l)$ is the original boundary expression and $a_n^{(0)}$ is the n^{th} Fourier coefficient of the original shape then:

- The change of starting point can be expressed as $z(l) = z^{(0)}(l+\tau)$ is a phase shift in the transform. The resulting Fourier coefficients become $a_n = e^{jn\tau}a_n^{(0)}$ which are invariant to the starting point shift.

- Assuming that shapes are centered about the origin of the coordinate system, then rotation around the origin with angle ϕ gives rise to the boundary expression $z(l) = z^{(0)}(l)e^{j\phi}$. As a result the invariant Fourier coefficients are $a_n = a_n^{(0)}e^{j\phi}$.

- Translation of a shape can be expressed as $z(l) = z^{(0)}(l)+c$, wherein only the zero-frequency component changes. This implies that Fourier coefficients are invariant to translation with the exception of the first coefficient which only reflects the mean position:

$$a_n = \begin{cases} a_n^{(0)} & n \neq 0 \\ a_n^{(0)} + c & n = 0 \end{cases}$$

- Scaling of a shape can be expressed as $z(l) = sz^{(0)}(l)$, such that it is a multiple of the Fourier coefficients and a constant: $a_n = s\,a_n^{(0)}$. This operation provides the means for scale invariance.

2.2 Fourier Transform of Boundary

The chain code described in Chapter 1 approximates a continuous contour in 2-D by a sequence of piecewise linear fits that consists of 8 standardized line segments $C = a_1, a_2, a_3 ... a_n$.

The time needed to traverse a particular link a_i of the chain code at a constant speed is given by:

$$\Delta t_i = 1 + (\frac{\sqrt{2}-1}{2})(1-(-1)^{a_i}) = \begin{cases} 1 & if \quad a_i \in \{0,2,4,6\} \\ \sqrt{2} & if \quad a_i \in \{1,3,5,7\} \end{cases}$$

The time required to traverse the first p links in the chain are:

$$t_p = \sum_{i=1}^{p} \Delta t_i$$

The changes in the x and y projections of the chain as the link a_i is traversed are:

$$\Delta x_i = sgn(6 - a_i)sgn(2 - a_i) = \begin{cases} 1 & if \quad a_i \in \{0, 1, 7\} \\ 0 & if \quad a_i \in \{2, 6\} \\ -1 & if \quad a_i \in \{3, 4, 5\} \end{cases}$$

$$\Delta y_i = sgn(4 - a_i)sgn(a_i) = \begin{cases} 1 & if \quad a_i \in \{1, 2, 3\} \\ 0 & if \quad a_i \in \{0, 4\} \\ -1 & if \quad a_i \in \{5, 6, 7\} \end{cases}$$

where

$$sgn(k) = \begin{cases} 1 & if \quad k > 0 \\ 0 & if \quad k = 0 \\ -1 & if \quad k < 0 \end{cases}$$

Locating the starting point of the chain code at the origin, the projections on x and y of the first p links of the chain are, respectively:

$$x_p = \sum_{i=1}^{p} \Delta x_i$$

$$y_p = \sum_{i=1}^{p} \Delta y_i$$

The Fourier series expansion for the x and y projections of the complete contour of the chain code $t \in [0, T]$ using the sinusoidal basis are defined as:

$$x(t) = A_0 + \sum_{n=1}^{\infty} (a_n cos\frac{2n\pi t}{T} + b_n sin\frac{2n\pi t}{T})$$

$$y(t) = C_0 + \sum_{n=1}^{\infty} (c_n cos\frac{2n\pi t}{T} + d_n sin\frac{2n\pi t}{T})$$

where the Fourier coefficients are:

$$A_0 = \frac{1}{T}\int_0^T x(t)dt \qquad C_0 = \frac{1}{T}\int_0^T y(t)dt$$

$$a_n = \frac{2}{T}\int_0^T x(t)cos\frac{2n\pi t}{T}dt \qquad b_n = \frac{2}{T}\int_0^T x(t)sin\frac{2n\pi t}{T}dt$$

$$c_n = \frac{2}{T}\int_0^T y(t)cos\frac{2n\pi t}{T}dt \qquad d_n = \frac{2}{T}\int_0^T y(t)sin\frac{2n\pi t}{T}dt$$

Fourier transform of the boundary $\Phi(t) = (x(t), y(t))$ represents the smooth form of the chain code $C = a_1a_2a_3...a_n$.

2.2.1 Elliptic Fourier descriptors

The elliptic Fourier decomposition is readily apparent when the projections are expressed in matrix form:

$$\begin{bmatrix} x(t) \\ y(t) \end{bmatrix} = \begin{bmatrix} A_0 \\ C_0 \end{bmatrix} + \sum_{n=1}^{\infty} \begin{bmatrix} a_n & b_n \\ c_n & d_n \end{bmatrix} \begin{bmatrix} cos\, nt \\ sin\, nt \end{bmatrix}$$

A geometric interpretation, in terms of ellipses, can be developed from this decomposition.The matrix $\begin{bmatrix} a_n & b_n \\ c_n & d_n \end{bmatrix}$ is a parametric form for an ellipse whereas a_n, b_n, c_n, d_n determine the characteristics of the ellipse. The ellipse of degree n is completely described by its vector path $\begin{bmatrix} cos\, nt \\ sin\, nt \end{bmatrix}$.The coefficients A_0, C_0 are the mean values of the coordinates and determine the overall translation of the geometric center of the closed contour. The parameters set$(A_0, C_0, a_n, b_n, c_n, d_n; n = 1..\infty)$ represents the elliptic Fourier descriptors.

The elliptic Fourier descriptors a_n and b_n corresponding to the n^{th} harmonic are given by:

$$a_n = \frac{T}{2n^2\pi^2}\sum_{p=1}^{K}\frac{\Delta x_p}{\Delta t_p}[cos\frac{2n\pi t_p}{T} - cos\frac{2n\pi t_{p-1}}{T}]$$

$$b_n = \frac{T}{2n^2\pi^2}\sum_{p=1}^{K}\frac{\Delta x_p}{\Delta t_p}[sin\frac{2n\pi t_p}{T} - sin\frac{2n\pi t_{p-1}}{T}]$$

$$A_0 = \frac{1}{T}\sum_{p=1}^{K}\frac{\Delta x_p}{2\Delta t_p}(t_p^2 - t_{p-1}^2) + \xi_p(t_p - t_{p-1})$$

where

$$\xi_1 = 0,\ \ \xi_p = \sum_{j=1}^{p-1}\Delta x_j - \frac{\Delta x_p}{\Delta t_p}\sum_{j=1}^{p-1}\Delta t_j$$

The elliptic Fourier descriptors c_n and d_n corresponding to the n^{th} harmonic are given by:

$$c_n = \frac{T}{2n^2\pi^2}\sum_{p=1}^{K}\frac{\Delta y_p}{\Delta t_p}[cos\frac{2n\pi t_p}{T} - cos\frac{2n\pi t_{p-1}}{T}]$$

$$d_n = \frac{T}{2n^2\pi^2}\sum_{p=1}^{K}\frac{\Delta y_p}{\Delta t_p}[sin\frac{2n\pi t_p}{T} - sin\frac{2n\pi t_{p-1}}{T}]$$

$$C_0 = \frac{1}{T}\sum_{p=1}^{K}\frac{\Delta y_p}{2\Delta t_p}(t_p^2 - t_{p-1}^2) + \delta_p(t_p - t_{p-1})$$

where

$$\delta_1 = 0,\ \ \delta_p = \sum_{j=1}^{p-1}\Delta y_j - \frac{\Delta y_p}{\Delta t_p}\sum_{j=1}^{p-1}\Delta t_j$$

Note that:

$$t_p = \sum_{j=1}^{p}\Delta t_j \qquad T = \sum_{p=1}^{K} t_p$$

$$\Delta t_p = \sqrt{\Delta x_p^2 + \Delta y_p^2} \quad \Delta x_p = (x_p - x_{p-1}) \quad \Delta y_p = (y_p - y_{p-1})$$

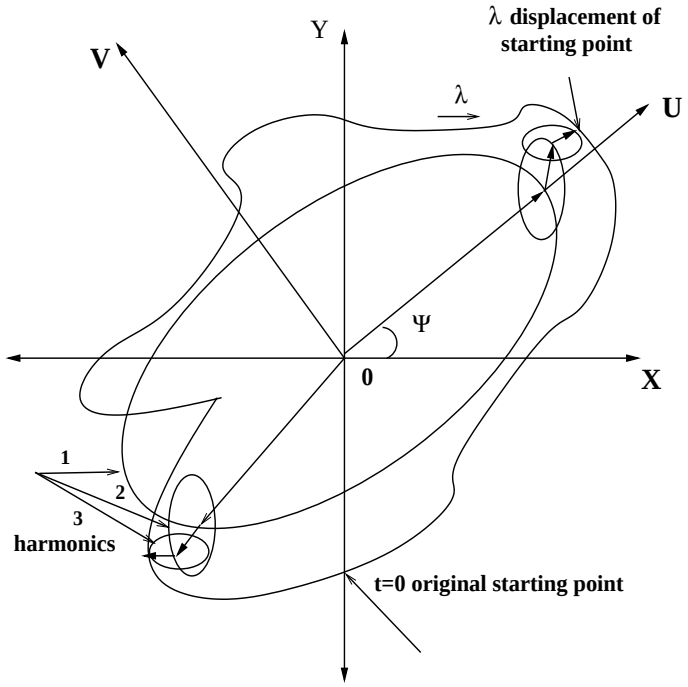

Figure 2.4: The first 3 phasors of the elliptic approximation to a contour

The curve can be viewed as a sum of rotating phasors, called harmonic loci, each individually defining an ellipse and rotating with a speed proportional to their harmonic number n. The larger the number of ellipses involved, the more accurate the representation becomes as showed in Figure 2.4

2.2.2 Normalization of Fourier descriptors

Each ellipse can be described by four geometric properties: semi-major axis length, semi-minor axis length, rotation and phase shift. The rotation is the angle from the x-axis to the major axis of the ellipse. The phase shift is the difference in phase from the major axis to the position of the starting point $t = 0$. Based only on the intrinsic geometric properties we describe an intuitive way of normalizing the Fourier coefficients a_n, b_n, c_n and d_n obtained in the previous subsection. The resulting Fourier descriptors

are invariant with regard to scale, rotation, translation and starting point on the contour.

Normalizing a Fourier contour representation means placing the first harmonic phasor of the Fourier series in a standard position. This means translating the origin of the X, Y coordinate system to the center of the first harmonic phasor and rotating the X, Y coordinate axes into a new U, V coordinate axes defined by the major and minor axes of the ellipse as showed in Figure 2.4

Consider the truncated Fourier series approximation to a closed contour:

$$x(t) = A_0 + \sum_{n=1}^{N} X_n(t)$$

$$y(t) = C_0 + \sum_{n=1}^{N} Y_n(t)$$

where the components of the projections $X_n, Y_n (1 \leq n \leq N), t \in [0, T]$ are

$$X_n(t) = a_n cos\frac{2n\pi t}{T} + b_n sin\frac{2n\pi t}{T}$$

$$Y_n(t) = c_n cos\frac{2n\pi t}{T} + d_n sin\frac{2n\pi t}{T}$$

A difference in the starting point, λ units in the direction of rotation around contour is displayed in the projected space as a phase shift and can be expressed as $X_n(t^* + \lambda)$.Expanding $X_n(t)$ and $Y_n(t)$ where $t = t^* + \lambda$

$$\begin{bmatrix} X_n^* \\ Y_n^* \end{bmatrix} = \begin{bmatrix} a_n^* & b_n^* \\ c_n^* & d_n^* \end{bmatrix} \begin{bmatrix} cos\frac{2n\pi t^*}{T} \\ sin\frac{2n\pi t^*}{T} \end{bmatrix}$$

we obtain a new set of coefficients a_n^*, b_n^*, c_n^* and d_n^* which compensate for the arbitrary position of the starting point. This is showed by introducing a rotational operator that relates Fourier coefficients at any starting point a_n, b_n, c_n and d_n to the coefficients $a_n^*, b_n^*, c_n^*$and d_n^* for another stating point displaced with λ.

$$\begin{bmatrix} a_n^* & b_n^* \\ c_n^* & d_n^* \end{bmatrix} = \begin{bmatrix} a_n & b_n \\ c_n & d_n \end{bmatrix} \begin{bmatrix} cos\frac{2n\pi\lambda}{T} & -sin\frac{2n\pi\lambda}{T} \\ sin\frac{2n\pi\lambda}{T} & cos\frac{2n\pi\lambda}{T} \end{bmatrix}$$

The rotation of X,Y coordinates axes through ψ degree into the U,V axes is accomplished by the rotational operation and the projections on U,V axes are:

$$\begin{bmatrix} u_n \\ v_n \end{bmatrix} = \begin{bmatrix} cos\psi & sin\psi \\ -sin\psi & cos\psi \end{bmatrix} \begin{bmatrix} X_n^* \\ Y_n^* \end{bmatrix}$$

Hence the two rotations are necessary to achieve the invariance to the axial rotation and a shift in the starting point. The combined effects, the invariant Fourier coefficients $a_n^{\#}, b_n^{\#}, c_n^{\#}$ and $d_n^{\#}$ can be expressed as:

$$\begin{bmatrix} a_n^{\#} & b_n^{\#} \\ c_n^{\#} & d_n^{\#} \end{bmatrix} = \begin{bmatrix} cos\psi & sin\psi \\ -sin\psi & cos\psi \end{bmatrix} \begin{bmatrix} a_n & b_n \\ c_n & d_n \end{bmatrix} \begin{bmatrix} cos\frac{2n\pi\lambda}{T} & -sin\frac{2n\pi\lambda}{T} \\ sin\frac{2n\pi\lambda}{T} & cos\frac{2n\pi\lambda}{T} \end{bmatrix}$$

Elliptic 1st harmonic locus

When the first harmonic locus is an ellipse the rotations are defined relative to the semi-major axis of the locus then produce two related representations of the contour:

$$\begin{bmatrix} a_n^{\#(1)} & b_n^{\#(1)} \\ c_n^{\#(1)} & d_n^{\#(1)} \end{bmatrix} = \begin{bmatrix} cos\psi_1 & sin\psi_1 \\ -sin\psi_1 & cos\psi_1 \end{bmatrix} \begin{bmatrix} a_n & b_n \\ c_n & d_n \end{bmatrix} \begin{bmatrix} cos\, n\theta_1 & -sin\, n\theta_1 \\ sin\, n\theta_1 & cos\, n\theta_1 \end{bmatrix}$$

whereas the other semi-major axis is further rotated by π:

$$\begin{bmatrix} a_n^{\#(2)} & b_n^{\#(2)} \\ c_n^{\#(2)} & d_n^{\#(2)} \end{bmatrix} = (-1)^{n+1} \begin{bmatrix} a_n^{\#(1)} & b_n^{\#(1)} \\ c_n^{\#(1)} & d_n^{\#(1)} \end{bmatrix}$$

The expression for the starting point displacement θ_1 can be determined by differentiating the magnitude of the first harmonic ($N = 1$) of the Fourier series (not including the bias terms A_0 and C_0):

$$S = \sqrt{x_1^2 + y_1^2} \text{ where}$$

$$x_1(t) = a_1 cos\theta + b_1 sin\theta$$

$$y_1(t) = c_1 cos\theta + d_1 sin\theta$$

$$\theta = \frac{2\pi t}{T}$$

Setting the derivative to zero:

$$\theta_1 = \frac{1}{2}\arctan\left[\frac{2(a_1 b_1 + c_1 d_1)}{a_1^2 + c_1^2 - b_1^2 - d_1^2}\right] \quad \theta_1 \in [0, \pi)$$

The expression of the rotation angle $\psi_1$is determined from a_1^* and c_1^* Fourier coefficients that are already correct for the starting point displacement θ_1. When the first harmonic phasor is aligned with the semi-major axis $t^* = 0$:

$$\psi_1 = \arctan\left[\frac{y_1^*(0)}{x_1^*(0)}\right] = \arctan\frac{c_1^*}{a_1^*} \quad \psi_1 \in [0, 2\pi)$$

Circular 1st harmonic locus

When first harmonic locus is a circle: $a_1^2 + b_1^2 + c_1^2 + d_1^2 = 2(a_1 d_1 - b_1 c_1)$, the rotations are made with the respect to the line defined by the centroid of the contour and the point on the contour most distal from the centroid (A_0, C_0). Since the most distal point p can be non-unique, k related representations can result, corresponding to k sets of Fourier coefficients, $p = 1..k$:

$$\begin{bmatrix} a_n^{\#(p)} & b_n^{\#(p)} \\ c_n^{\#(p)} & d_n^{\#(p)} \end{bmatrix} = \begin{bmatrix} cos\psi_p & sin\psi_p \\ -sin\psi_p & cos\psi_p \end{bmatrix} \begin{bmatrix} a_n & b_n \\ c_n & d_n \end{bmatrix} \begin{bmatrix} cos\, n\theta_p & -sin\, n\theta_p \\ sin\, n\theta_p & cos\, n\theta_p \end{bmatrix}$$

The starting point rotation θ_p is defined relative to the p^{th} most distant point:

$$\theta_p = \frac{2\pi t_p}{T} \quad \theta_p \in (0, 2\pi]$$

and the axial rotation angle ψ_p is:

$$\psi_p = \arctan\left[\frac{y_p - C_0}{x_p - A_0}\right] \qquad \psi_p \in [0, 2\pi).$$

Scale invariance is obtained by normalizing each Fourier coefficient by the magnitude of the semi-major axis $\sqrt{a_1^{*2} + c_1^{*2}}$ when the first harmonic locus is elliptic, and by the magnitude of radius$\sqrt{a_1^2 + c_1^2}$ when the first harmonic locus is circular.

Translation invariance is obtained by removing the bias terms A_0, C_0 from the Fourier series. This indicates that Fourier descriptors are invariant to translation except the first coefficient which only reflects the mean position.

The new parameters $(A_0, C_0, a_n^{\#}, b_n^{\#}, c_n^{\#}, d_n^{\#}, \theta_1, \psi_1 ...)$ are the invariant Fourier descriptors - FD and form a compact representation of the contour. A contour can be reconstructed from FD by the inverse Fourier transform. The low-frequency components or the low order harmonics of the Fourier descriptors capture the coarse representation of the boundary shape, whereas the high-frequency components or the higher order harmonics capture the finer details. Graphic examples of image contour is displayed with n- harmonic Fourier approximations in Figures 2.5 and 2.6.

2.3 Design and Methods

The image record can provide the information necessary to assess the cancer patient's initial presentation, staging of disease, therapy planning, response to treatment, and long-term follow-up for outcome assessment. Consequently, there is a tremendous need for tools for searching, retrieving and classifying medical images efficiently in order to take advantage of their rich information content. Querying an image database can be difficult and one of the main difficulties lies in designing appropriate features or descriptors to represent and organize constituent images. We have established a medical imaging database of delineated ventricles which were segmented from the MR images with each structure encoded using elliptic Fourier descriptors. In order to describe the closed surface of a delineated 3-D object (anatomic structure or tumor) we extended the 2-D elliptic Fourier descriptors to a 3-D descriptor by developing an algorithm which first computes elliptic Fourier descriptors across each horizontal cross-section, and then subsequently performs a Fourier transform across the resulting descriptors. The shape

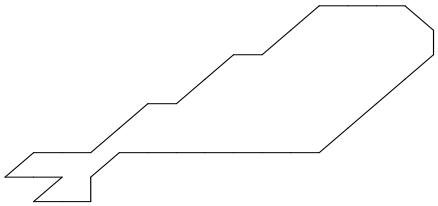

original contour

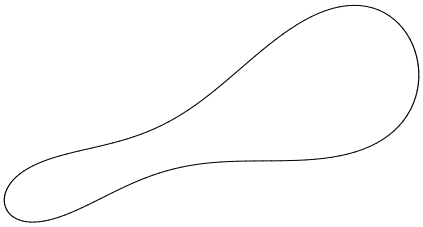

n=2 harmonics

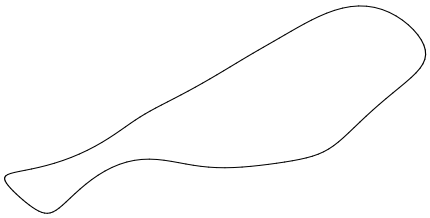

n=7 harmonics

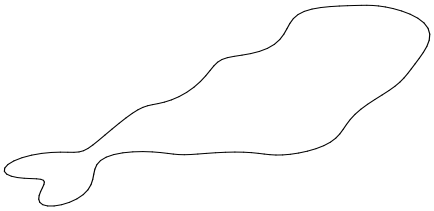

n=12 harmonics

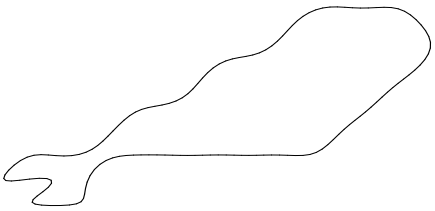

n=17 harmonics

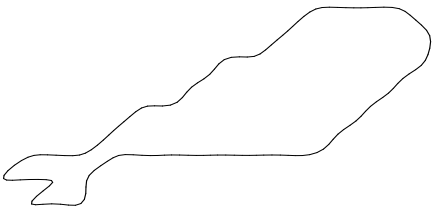

n=25 harmonics

Figure 2.5: n -harmonics Fourier approximation of a cross-section of a ventricle from MRI brain scan

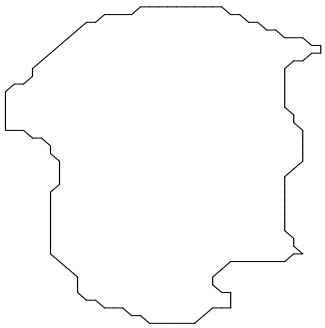

original contour

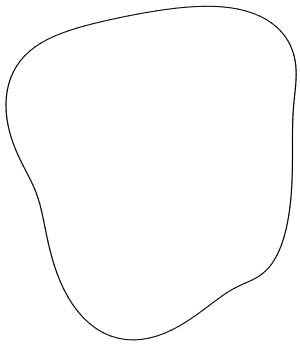

n=4 harmonics

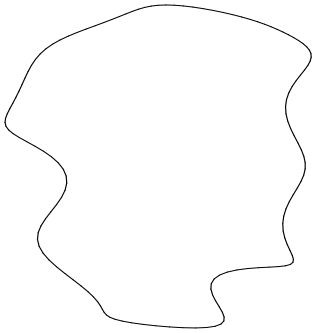

n=8 harmonics

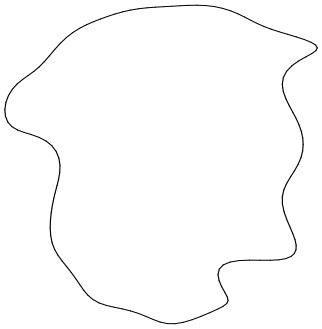

n=16 harmonics

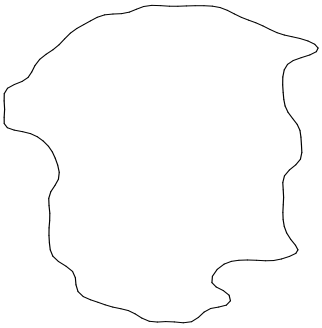

n=32 harmonics

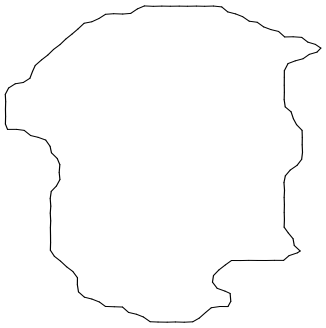

n=64 harmonics

Figure 2.6: n -harmonics Fourier approximation of a cross-section of a liver tumor from CT image scan

descriptors were used to provide a reliable, objective means for characterizing changes in shape and as a basis for conducting statistical comparisons of 3D objects. In order to achieve this capability it was necessary to develop and implement registration and re-section algorithms to correct for differences in patient positions during consecutive imaging studies.

2.3.1 Double Fourier Transform

An ordered set of cross-sections are sampled as a discrete representation of a continuous complex function $s_z(t)$, $0 \leq t \leq T$ which represents the closed surface of the delineated 3-D structure. The $X - Y$ Cartesian coordinates of the contour at the sampled points constitute the real and the imaginary parts of the complex function. T_z represents the contour length at height z and since $s_z(t)$ is given only at P sample points , $s_z(t)$ is sampled uniformly as:

$$t_p = pT_z/P \quad p = 0, 1, ..., P-1$$

For a fixed height z and a specific number n of harmonics, the Fourier descriptors $fd(n, z)$ are evaluated as:

$$fd(n,z) = \frac{1}{T_z}\int_0^{T_z} s_z(t)e^{-j2\pi nt/T_z}\,dt = \frac{1}{P}\sum_{p=0}^{P-1} s_z(t_p)e^{-j2\pi nt_p/T_z}$$

The inverse Fourier transform can be applied to the resulting descriptors and the reconstructed contour is then obtained:

$$s_z(t) = \sum_{n=-\infty}^{\infty} fd(n,z)e^{j2\pi nt/T_z}$$

In order to compute the shape variation of cross-sections along the z-axis, for the purpose of our studies, the Fourier transform was applied again, this time on $fd(n, z)$. The closed curves in the z-axis were generated by mirroring the Fourier descriptors $fd(n, z)$, where range of z is between 0 and K. Therefore, the contour length is uniformly sampled as:

$$z_q = qK/Q \quad q = 0, 1, ...Q-1$$

Taking in account that only Q cross-sections are possible, the new Fourier descriptors were evaluated as :

$$FD(k,z) = \frac{1}{K}\int_0^K fd(n,z)e^{-j2\pi kz/K}\,dz = \frac{1}{Q}\sum_{q=0}^{Q-1} fd(n,z_q)e^{-j2\pi kz_q/K}$$

Planar Fourier descriptors were subsequently reconstructed by inverse Fourier transform as follows:

$$fd(n,z) = \sum_{k=-\infty}^{\infty} FD(k,z)e^{j2\pi kz/K}$$

In this formulation the closed surface $s_z(t)$ was encoded in the shape descriptors by the double Fourier transform:

$$FD(k,z) = \frac{1}{QP}\sum_{q=0}^{Q-1}\sum_{p=0}^{P-1} s_z(t_p)e^{-j2\pi(kz_q/K+nt_p/T_z)}$$

and the reconstructed closed surface was obtained based on these shape descriptors as:

$$s_z(t) = \sum_{n=-\infty}^{\infty}\sum_{k=-\infty}^{\infty} FD(k,z)e^{j2\pi(kz/K+nt/T_z)}$$

Since the double Fourier transform is a reversible linear transformation all the shape information is captured and preserved in the descriptors.

2.3.2 Registration of 3-D objects

The registration process takes as input two (or more) images: one image is considered as the reference (or the data) image and the other one is the deformable (or the model) image. Given two sets of 3-dimensional points: data $D = \{d_p\}$ and model $M = \{m_k\}$, for each data point $d_i \in D$ it is necessary to find the index j of the corresponding point

$m_j \in M$ then recover the transformation $m_j = d_i + f(d_i)$ which aligns the corresponding points while minimizing some objective error function $E(d_i, m_j)$.

Suppose that the shapes of two different 3-D data sets are given by N points as measured in two different Cartesian coordinate systems - $p_{a,i}$ in system A and $p_{b,i}$ in system B, $1 \leq i \leq N$. Registration or the transformation between two Cartesian coordinate systems, can be thought of as a result of a rigid motion and thus, can be decomposed into rotations and translations. The Iterative Closest Points - ICP [34] aims to find the optimal set of transformations that register the two 3-D shapes by minimizing the sum of squares of residual errors between them:

$$e(R,t) = \sum_{i=1}^{N} || \, p_{a,i} - sR(p_{b,i}) - t \, ||^2$$

where R is the rotation transformation, s the scaling factor and t the translation. This iterative method is applied repeatedly until the change produced by the transformation becomes negligible.

The ICP algorithm allows freedom in the implementation of the closest point determination (minimum distance) and in the way of finding the optimal transformation in each iteration step. Any optimization method such as steepest descendent, conjugate gradient, singular value decomposition (SDV) or unit quaternion algorithm can be used to find the least squares rotation R, scale s and translation t. The difficult part of the problem is finding the rotation R. We implemented the closed-form solution [35] in which unit quaternions are used to represent the optimal orientation R. The closed-form solution has the advantages that it provides the best possible transformation in a single step and that is no need to find a good initial guess as in iterative methods.

A quaternion is a vector with four components $q = [q_0, q_1, q_2, q_3]^T$, a scalar q_0 and an ordinary vector [35]. Any orientation can be represented by a single axis of rotation and a single angle. The unit quaternion specifies a rotation from its reference position through an angle $\theta = 2 \, arccos \, q_0$ around the rotation axis $(q_1, q_2, q_3)^T$.The representation of an orientation is in the form of quaternion:

$$q = [cos\frac{\theta}{2}, sin\frac{\theta}{2}(q_1, q_2, q_3)]$$

The rotation is performed by multiplying together quaternions representing the axis of rotation and the final resulting quaternion is then converted to the desired rotation matrix R:

$$R = \begin{bmatrix} q_0^2 + q_1^2 - q_2^2 - q_3^2 & 2(q_1 q_2 - q_0 q_3) & 2(q_1 q_3 + q_0 q_2) \\ 2(q_2 q_1 + q_0 q_3) & q_0^2 + q_2^2 - q_1^2 - q_3^2 & 2(q_2 q_3 + q_0 q_1) \\ 2(q_1 q_3 - q_0 q_2) & 2(q_2 q_3 + q_0 q_1) & q_0^2 + q_3^2 - q_1^2 - q_2^2 \end{bmatrix}$$

We can summarize the algorithm for finding the rotation matrix. Both sets of points, p_a and p_b are translated to their centroids c_a and c_b and from now one we deal with these measurements: $p'_{a,i} = p_{a,i} - c_a$ and $p'_{b,i} = p_{b,i} - c_b$. For each pair of coordinates we compute the nine possible products $x'_a x'_b, x'_a y'_b, x'_a z'_b ... z'_a z'_b$ then the sums $S_{xx}, S_{xy}, S_{xz} ... S_{zz}$ where:

$$S_{xx} = \sum_{i=1}^{N} x'_{a,i} x'_{b,i}$$

The elements of the real symmetric $4\,X\,4$ matrix K are sums of products of coordinates measured in the A system with coordinates measured in the B system and is defined as [35]:

$$K = \begin{bmatrix} S_{xx} + S_{yy} + S_{zz} & S_{yz} - S_{zy} & S_{zx} - S_{xz} & S_{xy} - S_{yx} \\ S_{yz} - S_{zy} & S_{xx} - S_{yy} - S_{zz} & S_{xy} + S_{yx} & S_{zx} + S_{xz} \\ S_{zx} - S_{xz} & S_{xy} + S_{yx} & -S_{xx} + S_{yy} - S_{zz} & S_{yz} + S_{zy} \\ S_{xy} - S_{yx} & S_{zx} + S_{xz} & S_{yz+S_{zy}} & -S_{xx} - S_{yy} + S_{zz} \end{bmatrix}$$

To find the rotation that minimizes the sum of squares of errors $e(R,t)$, it is necessary to find the unit quaternion q that maximizes

$$q^T K q$$

The solution for the desired quaternion is the eigenvector corresponding to the most positive eigenvalue of the matrix K [35]. The eigenvalues are obtained by solving the forth-order polynomial equation $det(K - \lambda I) = 0$ where I is the $4\,X\,4$ identity matrix. After we select the largest positive eigenvalue λ_m the corresponding eigenvector e_m is

founded by solving the equation $[K-\lambda_m I]e_m = 0$. The quaternion representing rotation is a unit vector in the same direction with eigenvector e_m.

In order to find translation t [35] the error term to be minimized can be written as:

$$e(R,t) = p_{a,i} - sR(p_{b,i}) - t = p'_{a,i} - sR(p'_{b,i}) - t'$$

where $t' = t - c_a + sR(c_b)$, therefore the sum of the squares errors becomes:

$$e(R,t) = \sum_{i=1}^{N} || \, p'_{a,i} - sR(p'_{b,i}) - t' \, ||^2$$

which is minimized with $t' = 0$ or

$$t = c_a - sR(c_b)$$

The translation is just the difference between the centroid of the coordinates in one system and the rotated and scaled centroid of the coordinates in the other system.

The above formulation of the error term leads to an asymmetry in the determination of the optimal scale factor. The "optimal " transformation from A to B coordinate system is not the exact inverse of the "optimal " transformation from B to A coordinate system.[35] Using a symmetrical expression for the error term:

$$e(R,t) = \frac{1}{\sqrt{s}} p'_{a,i} - \sqrt{s} R(p'_{b,i})$$

allows finding the scale transformation without the need to find the rotation as:

$$s = \sqrt{\frac{\sum_{i=1}^{N} ||p'_{a,i}||^2}{\sum_{i=1}^{N} ||p'_{b,i}||^2}}$$

The scale is equal to the ratio of the root-mean-square deviations of the coordinates from their centroids in the two systems.

Iterative Closest Point (ICP) algorithm

The iterative closest point algorithm (ICP) is able to register a "data" shape P with N_p points to a "model" shape X with N_x primitives [34]. The model shape may be represented in any of the allowable form such as point sets, line sets, triangle sets,

parametric curves, but for our purposes the model shape was decomposed into a point set. The method finds the nearest positions on one surface to a collection of points on the other surface and then transforms one surface so as to minimize the collective distance. This procedure is iterate until convergence.

The distance $d(p, X)$ between an individual point p and the set points $X = \{x_i\}$, $i \in \{1..N_x\}$ is defined as the Euclidean distance:

$$d(p, X) = min_{i \in \{1...N_x\}} ||p - x_i||$$

Let Y denote the resulting set of closest points that yields the minimum distance , and let C be the closest point operator $Y = C(P, X)$. The least squares registration is computed and let Q denote the quaternion operation. Given the resultant corresponding point set Y and the data set P , equation $(q, d_m) = Q(P, Y)$ means that q is the registration vector that best aligns P and Y, where d_m is the point matching mean square error in this alignment [34]. The registration vectors are defined relative to the data set P thus the final registration represents the complete transformation. If a tolerance $\tau > 0$ and an initial registration q_i are given the following steps of the ICP algorithm are applied until convergence:

1. Compute the closest points $Y_k = C(P_k, X)$.
2. Compute the registration $(q_k, d_k) = Q(P, Y_k)$.
3. Apply the registration $P_{k+1} = q_k(P)$.
4. If $(d_{k-1} - d_k) < \tau$, terminate. Else increase k and go back to step 1.

ICP has the objective of registering data that does not necessarily have the same number of points as the model, and more importantly, data whose points doesn't have a point to point association with the model.

2.3.3 Object classification

In our experiments the 2D elliptic Fourier transform was applied to each section to perform a section by section comparison of 3D objects. We describe the two distances,

ICP distance and Fourier distance used for object comparison and their related issues.

ICP distance is the distance resulting from the ICP registration algorithm, as the "best" distance between the data and the model. The distance is computed for each data point by searching for the closest point on the model, and averaged over the number of points. The measure of similarity is obtained by running ICP with different starting points and taking the best (minimum) value. The reason for the different starting points is that ICP is known to fall in local minima. The iterative operation used by ICP overlaps the two objects through rotation and a scale transformation, thus achieving a local maximum similarity between data and model. The problem with this method is that not only is very expensive computationally, but also requires the expansion of the object to 3D format.

The Fourier distance between two cross sections is defined as the Euclidean distance between their Fourier descriptors. The Fourier distance was used by Ferrario V. F and Sforza C. [36] to analyze sex and age shape differences of corpus callosum in childhood. The Fourier distance between two objects is the weighted average of distances between corresponding cross-sections. Comparing objects just based on their Fourier descriptors has only a complexity linear in the number of harmonics, and is therefore desirable for large objects that are encoded with few harmonics, a condition satisfied by the objects in our database.

In order to verify that this method can be used for classification purpose, we compare its behavior against the well known, and more intuitive ICP distance. To verify the correspondence between the two distances, we use a non-parametric (distribution-free) rank statistic proposed by Spearman in 1904 [37]. The Spearman rank correlation coefficient, that is 1 for complete agreement and -1 for disagreement is defined by:

$$r = 1 - \frac{6}{n^2 - 1}\left(\frac{\sum_i d_i^2}{n}\right)$$

where d_i represent the difference in statistical rank (the ordinal number of a value in a list arranged in a specified order) and n number of objects. The coefficient is used to measure the strength of correlation between two sets of data. Consequently we compared a query cross-section with 32 cross-sections from 11 different objects from

the database and the resultant rank correlation coefficient is 0.94. Thus, 2D Fourier descriptors have the potential to accurately characterize the shape and can be used to conduct a systematic section by section classification of 3D objects.

2.4 Results

2.4.1 Data Compression

The fact that the double Fourier descriptor transformation is reversible makes it possible to utilize it as a means for efficient storage of delineated objects. The reliability and accuracy with which Fourier encoding process captures the essence of the shape of an object is characterized by the number of harmonics used for xy encodings of the cross-sections, $(a_{zn}, b_{zn}, c_{zn}, d_{zn})$, and number of harmonics on z for the encoding of $A(a_{iz}, z), B(b_{iz}, z), C(c_{iz}, z)$ and $D(d_{iz}, z)$. The number of harmonics required for Fourier reconstruction depends on the complexity of the scanned data and the requirements of the application.

Experiments were conducted to determine the optimal number of harmonics required for reconstructions. The original (interactively traced) contour of the object of interest, brain structure or tumor, is defined by the data points

$$P^{-} = [x_i, y_i, z_i],\ i = 1..p$$

and the n harmonic Fourier approximation of the contour of the object $s_z(t) = (x(t), y(t))$ were superimposed. Since the original contour is given only at p points, the objects were reconstructed at a very high resolution - $p = 1000$ points for each cross-section. The centroid and the scale of each cross-section of the object is defined as:

$$c = \frac{1}{p}\sum_{i=1}^{p} P_i \quad scale = \sqrt{\frac{1}{p-1}\sum_{i=1}^{p} ||P_i - c||^2}$$

The measure of accuracy was defined by subtracting the n harmonic Fourier approximated contour from the original contour at specific sample points. The average Euclidean error was computed as:

$$\epsilon = \frac{1}{p * scale} \sum_{i=1}^{p} min_{t \in T_z} ||P_i - s_z(t)||_2$$

The graphs of the average error versus number of harmonics on xy and z are shown in Figure 2.7.

Based upon these studies it was determined that shape description was sufficiently stable using only the first 12 harmonics on xy and 32 harmonics on z, respectively. The Fourier series for subsequent analysis was truncated at this number of harmonics, accordingly since it was shown that most of the dimensional information was captured by the low order descriptors. The low order harmonics encodes the coarse representation of the three-dimensional object, whereas the higher harmonics adds details of object surface. Figure 2.8 shows the object reconstructions which are produced by varying the degree of approximation.

The data reduction effect of performing elliptical Fourier transform is illustrated in the following example. If delineated objects consists of 100 sections, on average, with 100 points for each section, about 30000 numbers would be required to store the x, y, z coordinates for all 100 points. In contrast, using 12 x 32 harmonics -representation of the same object would require 12 x 32 x 4=1536 numbers which was shown to contain enough detail to restore the object with high accuracy. Fourier encoding provides a form of lossy compression, as a result, each object is described by a set of descriptors and can be reliable reconstructed with adjustable degree of approximation.

2.4.2 Surface reconstruction

MR images were obtained from Laurie Imaging Center (UMDNJ - RWJ Medical School) and were acquired via 1.5 Tesla GE Sigma scanner. Each cross-sectional MR image was displayed on a high resolution screen while object contours were manually traced using Analyze AVW software (Mayo Foundation, Rochester Minnesota). The boundary of each anatomical structure (ventricle or tumor) was delineated based upon the intensity value of a particular voxel relative to the intensities of each neighboring voxel as shown in the Figure 2.9.

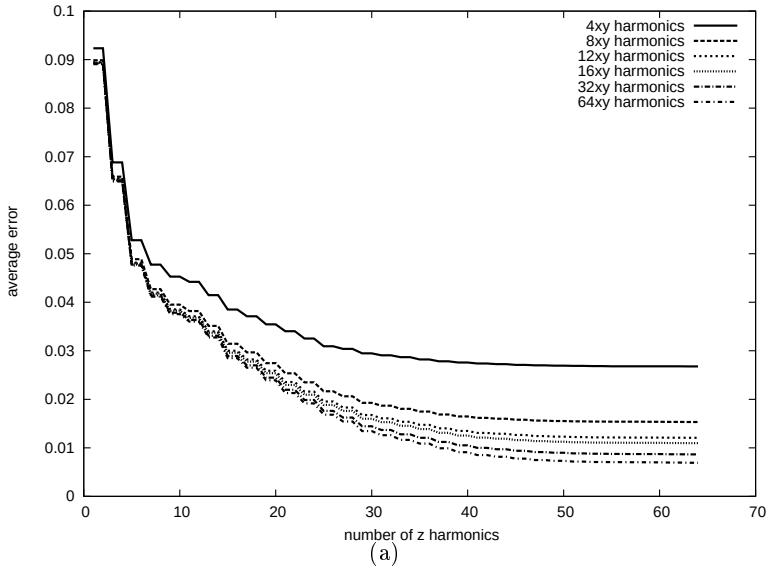

(a)

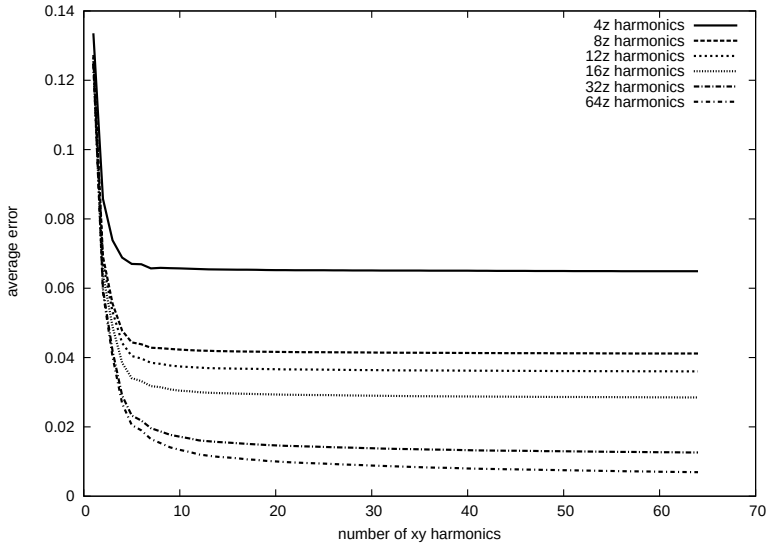

Figure 2.7: Average error versus harmonic content: a) on xy b) on z

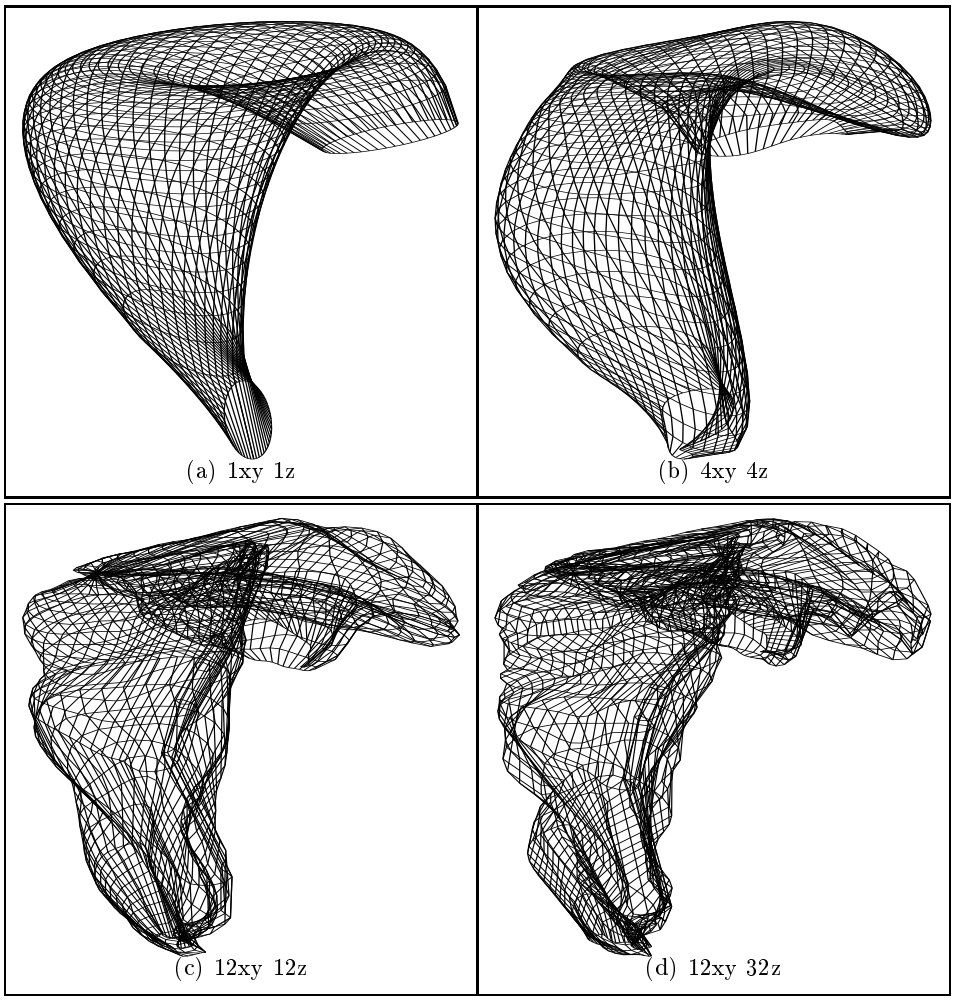

Figure 2.8: Fourier reconstruction of the normal left ventricle with different number of harmonics

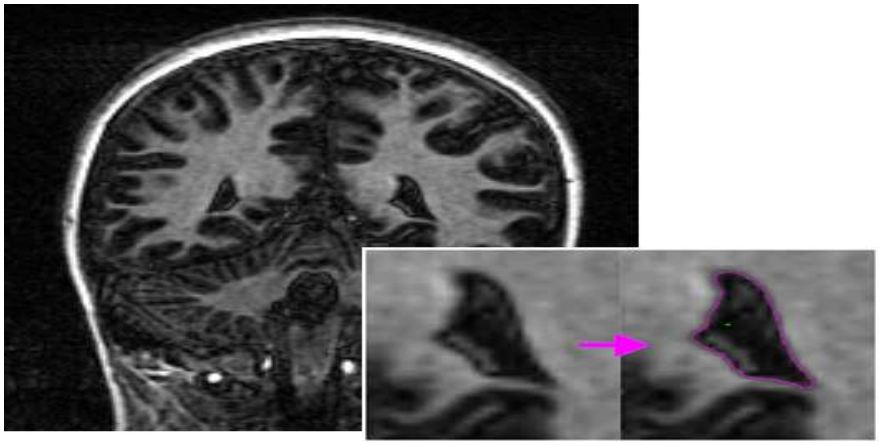

Figure 2.9: Analyze AVW - boundary tracing of the left ventricle

Sometimes due to variations in image resolutions the resulting trace of the boundary is not smooth. In regions exhibiting sudden changes in curvature, the resulting shape of the traced boundary presents a sawtooth form. In contrast by performing forward and reverse transformation through Fourier decomposition the resulting contours are smoothed considerably. Through systematic performance studies it was shown that the area of an object is encoded in a small number of harmonics, whereas the perimeter requires a large number of harmonics to achieve good accuracy as shown in the Figure 2.10 (c), respectively (d).

In the reconstruction process the degree of interpolation can be controlled not only in the cross-sections but also inter-cross-sections and the reconstructed volume is consequently more accurately represented. Figure 2.11 shows the reconstructed volume of the left ventricle (42 sections) for Bipolar disease using the same number of harmonics on xy - 12.

In order to provide more realistic anatomical surfaces representations Figure 2.12 shows an example of a double elliptic Fourier reconstruction of the ventricle for Asperger's Syndrome with different degrees of interpolation (the original ventricle has 40 sections).

2.4.3 Registration

The registration procedure was performed for all objects before they were added to the database. Figure 2.13 shows in two views the results of registration of a control left ventricle with a Bipolar left ventricle. The number of points in the "data" set (the Bipolar ventricle) is $N_p = 583$ and the number of points in the "model" set (the control ventricle) is $N_x = 537$. After 32 iterations if the tolerance value was $\tau = 0.001$ then the mean square error of the alignment was $d_m = 0.000001$. If $R^{3x3} = \{r_{ij}\}$ is the rotation transformation, s the scale factor and t the translation, the resulted registration matrix for the two ventricles is:

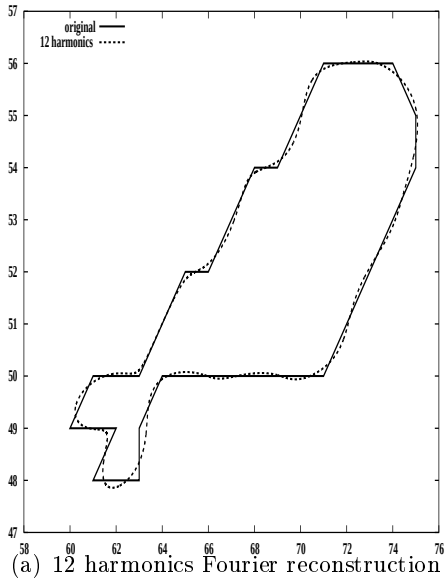

(a) 12 harmonics Fourier reconstruction

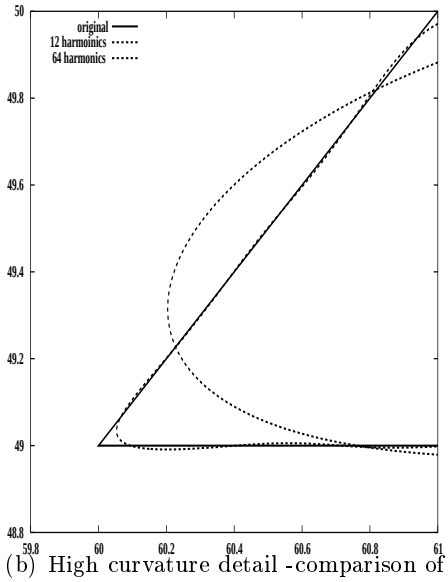

(b) High curvature detail -comparison of the original, 12 and 64 harmonics Fourier reconstruction

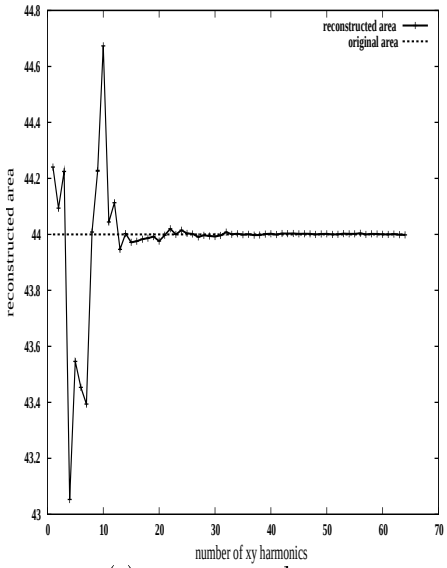

(c) reconstructed area

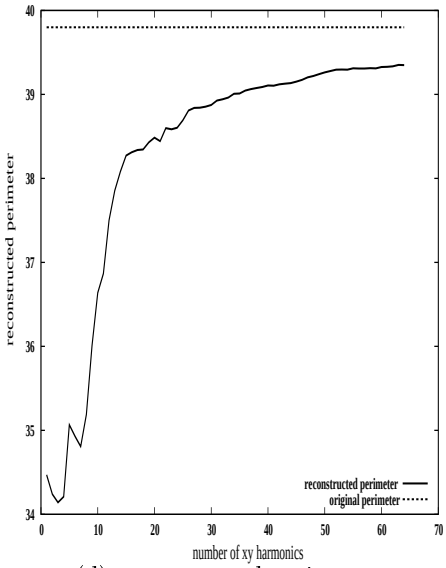

(d) reconstructed perimeter

Figure 2.10: Normal ventricle section - reconstructed area and perimeter versus xy harmonic content

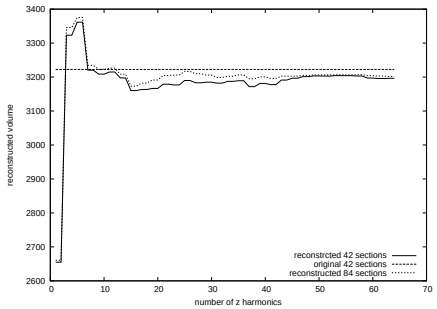

Figure 2.11: Bipolar ventricle - reconstructed volume versus z harmonic content

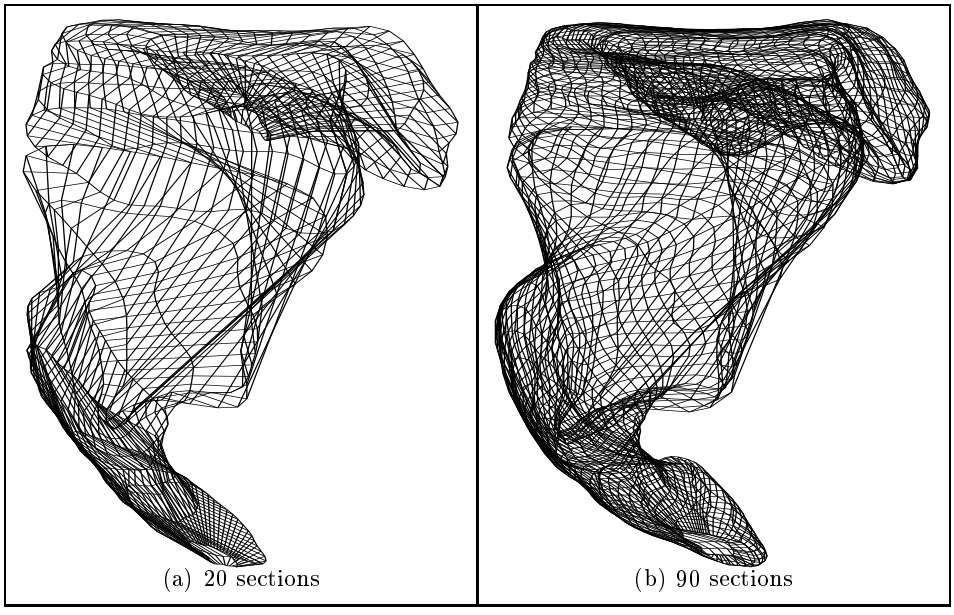

(a) 20 sections (b) 90 sections

Figure 2.12: Left ventricle Asperger's Syndrome - Fourier reconstruction with different degrees of interpolation on z

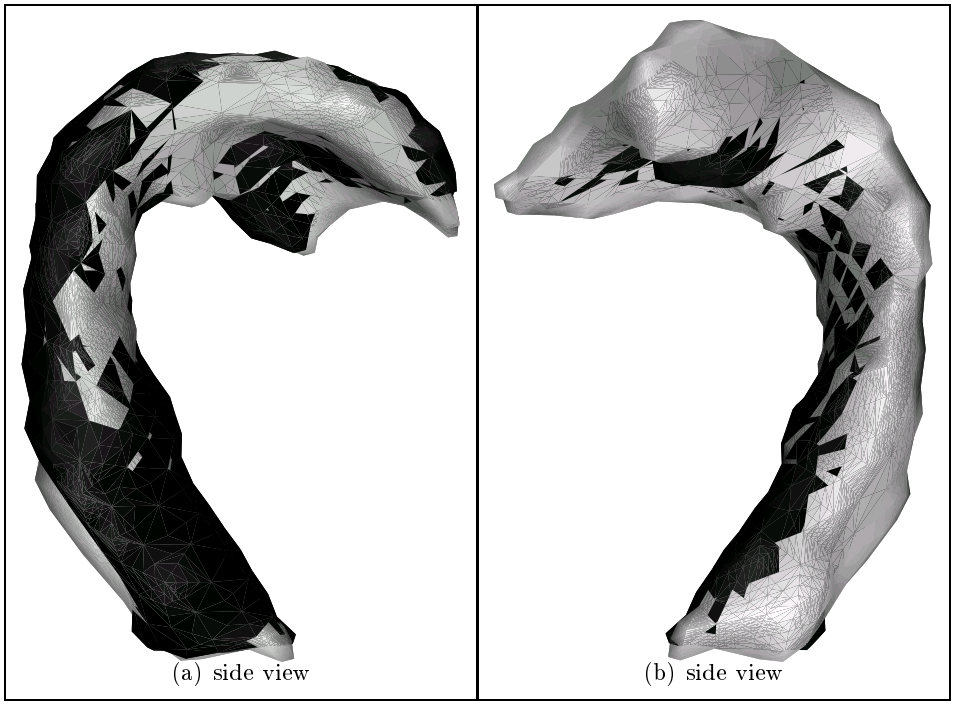

Figure 2.13: Registration of a control (gray) ventricle with a Bipolar (black) ventricle

$$T = \begin{bmatrix} sr_{11} & sr_{12} & sr_{13} & t_x \\ sr_{21} & sr_{22} & sr_{23} & t_y \\ sr_{31} & sr_{32} & sr_{33} & t_z \\ 0 & 0 & 0 & 1 \end{bmatrix} = \begin{bmatrix} 0.972938 & 0.103696 & -0.206492 & 18.663481 \\ -0.120967 & 0.989982 & -0.072817 & 14.552237 \\ 0.196873 & 0.095825 & 0.975735 & -9.652912 \\ 0 & 0 & 0 & 1 \end{bmatrix}$$

2.4.4 Re-section

Our object comparison procedure (distance defined on the object space) relies on planar closed curves that were obtained from sectioning along the same axis. It is not meaningful to compare sections from different objects unless they are taken at the same height along the same perpendicular axis. Usually sections obtained from the MRI procedure might use slightly different axis due to variations in positioning of the patient or another technical aspects. The re-section procedure recreates the outer hull of the object based on the initial sections, and then creates new parallel plane sections perpendicular on the desired axis. This change in the sectioning axis comes with some resolution loss,

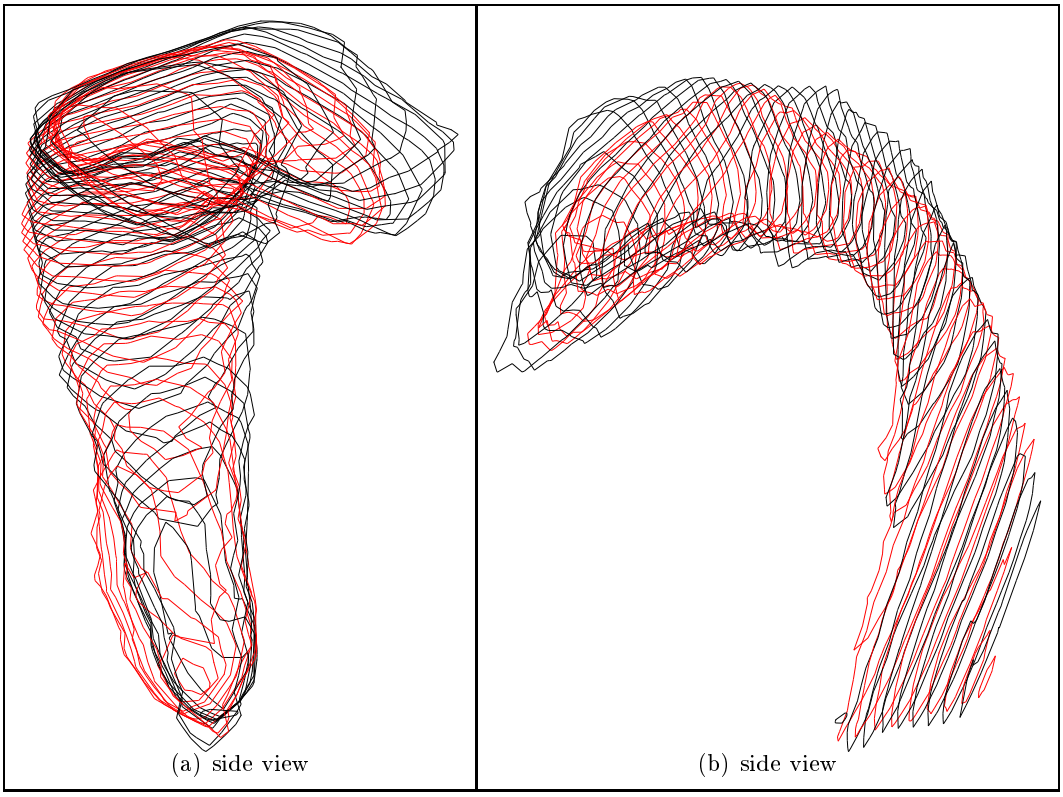

Figure 2.14: Re-section of a control (black) ventricle with a Bipolar (red) ventricle

but produces cross-sections that are comparable as 2D objects. This is a pre processing phase and is performed only once, at the time when the object is added to the database. Figure 2.14 shows in two views the results of re-section algorithm of a control left ventricle with a Bipolar left ventricle.

2.4.5 Database Architecture

The 3D medical imaging system features client-server architecture. The client part is intended to be used by remote clinical research sites to access the database at the server site. The server is designed to permit simultaneous access of several clients to the database. At the server site the incoming data is be registered, re-sectioned, encoded to elliptic Fourier descriptors and saved as a new entry in the database. The client retrieves the Fourier encoding of the object from the server, as a result of a query and performs local reconstruction for 3D visualization and other measurements. Multiple tools are

available for visualization slice by slice or volume, quantitative measurements and statistical analysis are be performed at the client site. The system supports distributed archiving and visualization of objects over a TCP/IP network.

2.5 Summary

The shape descriptor presented has been shown to reliably represent and reconstruct anatomic structures from cross-sectional contours. The coefficients derived in computing this shape characteristics were implemented using a double elliptic Fourier transform which provides a compact representation of the delineated structure. The medical imaging database that was presented has three main features:

- Compression: the algorithms that we utilized have the potential of compressing image based information while preserving the essential shape characteristics of the anatomic structures.
- Efficient querying: while the preliminary results were conducted utilizing a limited size database, it appears that 3D object classification methods based on Fourier descriptors provide the same accuracy as slower more computationally intensive methods, such as Iterative Closest Point.
- Distributed access: the prototype feature a TCP/IP based client-server architecture which divide the tasks between clients which perform visualizations and statistical operations, and a centralized server which services queries and performs data pre processing including registration and re-section. Preliminary results on a brain scan database shows promising archival and classification performance.

Our findings suggest the potential benefit of including shape descriptors for improved accuracy of differential diagnoses and clinical assessment.

2.5.1 Future work

Having developed and evaluated the fundamental algorithms and methodology a natural extension of this work includes the development of algorithms for 3-D object recognition

based on fully automated 3-D Fourier analysis. Another long-term goal of this project is to integrate the software with a relational database and develop tools for improved visualization and statistical analysis to construct as a tool for clinical assessment and diagnosis.

The development of algorithms which reliably perform automated segmentation of imaged liver studies using a mean-shift clustering approach has already begun. In the next phase of development a database of delineated liver lesions will be established, and 3-D Fourier descriptors will be generated to determine the reliability of the system for detecting and assessing volumetric and shape changes of tumors over the course of longitudinal studies.

Chapter 3

Liver Therapy Evaluation

3.1 Related Work for Registration in Medical Imaging

Medical imaging is essential for a range of clinical activities including rendering a diagnosis, staging disease progression, assessing response to treatment, and for surgical planning. Registration is the process of matching two or more images (or volumes) with one another. These images may have been obtained at different times from different scanners or from different viewpoints. Registration requires a spatial transformation, so that each location in one image can be mapped to the corresponding location in the second image. A combination of four key components are identified in the development of the any registration algorithm: a feature space, where features to be matched are selected, a transformation model, a similarity measure and an optimization module. The goal is to find an optimal transformation that provides the maximum similarity between images.

Medical image registration has been the topic of extensive research because of its importance in various application areas as well as of its complex nature. Maintz and Viergever classified the medical image registration methods [38] according to a model based on nine different criteria, which will be briefly explained in the Table 2.

In general, similarity between images can be classified into feature-based methods, intensity methods and a combination of the two approaches . Geometric or feature-based methods rely on reliably extracting and matching salient anatomical structures such as point landmark points, curves and surface information in order to define the transformation from one image set to an other. The algorithm for feature matching iteratively updates the transformation parameters and the corresponding solution. Intensity or voxel-based methods are used directly to match image intensities by operating

Table 3.1: Criteria for registration classification

Criteria	Subdivisions		
Dimensionality	Spatial dimensions: 2D/2D, 2D/3D, 3D/3D		
	Time series/spatial dimensions: 2D/2D, 2D/3D, 3D/3D		
Registration basis	Extrinsic	Invasive	Stereo tactic frame
			Fiducials (screw markers)
		Non-invasive	Mould, frame, dental
			Fiducials (skin markers)
	Intrinsic	Landmark based	Anatomical
			Geometrical
		Segmentation based	Rigid
			Deformable
		Voxel property based	Scalars/vectors
			Full image
	Non-image		
Nature of transformation	Rigid		
	Affine		
	Projective		
	Curved		
Domain of transformation	Local		
	Global		
Degree of user interaction	Interactive	Initialization supplied	
		No initialization supplie	
	Semi-automatic	User initialization	
		User sterring/correcting	
		Both	
	Automatic		
Optimization procedure	Parameters computed		
	Parameters searched for		
Modalities involved	Mono modal		
	Multimodal		
	Modality to model		
	Patient to modality		
Subject	Intrasubject		
	Intersubject		
	Atlas		
Structure imaged	Head		
	Thorax		
	Abdomen		
	Limbs		
	Pelvis and perineum		
	Spine and vertebrae		

on the whole image and are generally semi-automatic. To make the registration process more robust and to allow user interaction hybrid methods are developed. Each of these methods are discussed in greater detail in the following comprehensive surveys [38, 39, 40, 41, 42, 43, 44]. There is no single method which outperforms all other methods and which can be used in all situations. The registration result is always a trade-off between accuracy and speed.

The pioneering work of Terzopoulos et al. [45] and Bacjsy & Kovacic [46] have shown the advantages of introducing physics-based models to simulate volumetric deformation. The physics-based deformable surface models do not use any similarity measures explicitly and, feature matching and mapping function steps of the registration procedure are done simultaneously. The basic idea is to model an object while tracking it over time until achieving equilibrium between internal forces as defined by physical material properties, and external constrains based on the initial and final states of the object. One of the most widely used physical methods is the mass-spring model, which is a discrete representation of matter consisting of nodes connected by elastic links [58, 59, 60, 61]. Although real- time performance can be achieved using a mass-spring model, the behavior can often be unstable and unrealistic. Mass-spring methods are often used for surgery simulations due to their lower computational complexity and simplicity [63, 64]. More realistic deformable 3-D models are achieved by introducing continuum mechanics for linear elasticity. Linear elastic and visco-elastic registration models have been extensively described in the literature. The particular behavior of an elastic body is a function of both the internal stress and strain and the external forces applied, according to the physical principles. Broit [47] was the first to study elastic registration, where the images were viewed as two different observations of an elastic body, one before and one after the deformation. The displacement of the elastic body is derived using a linear elasticity model. A survey on elastic registration methods with emphasis on landmark-based schemes has been presented by Roth [48]. In the visco-elastic framework the Navier-Stokes viscous-fluid partial derivative (PDEs) equations describing the physical medium are solved on a discrete partial grid. This model, introduced by Christensen [49, 50] and Bro-Nielsen [51, 52] is topology preserving and gives excellent

results allowing both large displacements and nonlinearities. Unfortunately, this continuous transformation it is no longer guaranteed when solving the PDE on the discrete image grid. The visco-elastic model proved to be faster than optical flow based force model [53]. Other possible physics-based models include tensor-mass methods [54, 55] which allows real-time topology changes and implicit surfaces [62]. Picinbono et. al [56, 57]. This approach was developed an extension of tensor-mass method integrating geometrical non-linearity, which is a requirement for most surgical applications such as cutting, tearing or perforating.

The most widely used representations for deformable volumes are parametric models with thin plates-splines representation [65] and finite element models (FEM) introduced for computer engineering by Zienkiewicz [66]. Finite element methods (FEM) are used to find an approximation for a continuous equilibrium equation. In FEM framework, the surface´s mesh of the deformable object is decomposed into discrete finite elements joined at discrete node points. The 3D displacement of any element´s point is approximated as a linear combination of the components of the interpolation functions applied to the node displacements. An equilibrium expression is derived for each element and is assembled in a large and sparse linear system which has to be solved. The finite element model approach to the numerical solution of deformable surface models was first introduced by Terzopoulos & Metaxas [67] and later by McInerney & Terzopoulos [68]. Finite element analysis is a powerful computational tool for modeling soft tissue deformations. An extensive amount of research has yielded positive results for intra-patient nonrigid image registration by using biomechanics and finite element models (FEM) in neurosurgery [71, 72, 73, 74], breast [75, 76, 77], prostate [78, 79, 80], heart's ventricle [81, 82] as well as in radiotherapy settings [83, 84] .

In the context of liver therapy, several image registration methods has been investigated for alignment of serial data sets. Previous research has shown that the magnitude of liver deformation is typically 10-30 mm during relaxed respiration [85, 86]. To account for motion and deformation of the liver caused by respiration research has been done to register sparse intra operative ultrasound data to preoperative images of the liver using statistical models [87] and intensity-based methods [88]. Boes group [89]

have attempted to generate a geometric patient specific liver model by using manually identified anatomic landmarks and thin-plate splines, which could be matched to a standard liver using the same registration technique. Unfortunately, this method based on a normalized surface model requires substantial user interaction and has the limitation of using discrete landmarks rather than volumetric data. Recently finite element method (FEM) has been investigated in creating a biomechanical model of the liver [90], in multi-organ deformable image registration [91], for intra-operative soft tissue deformation of the liver using incomplete surface data [92]. A FEM was used to simulate the differences in distribution of temperature and the electric field potential at the end of a 12 min radiofrequency ablation procedure [93].

There have been many liver deformation studies, but only few have been reported on tracking metastases and primary tumors in the liver. Charnoz et al. [94] registered the segmented vascular network of the liver for the follow-up of tumor evolution. However, the blood vessel branch points are difficult to identify when different acquisition times are used and registering the vascular system alone does not take in account any information regarding surface liver deformation. Carrillo et al.[95] used a rigid intensity-based algorithm to perform registration of MR liver images acquired before thermal ablation and following treatment and reported an accuracy of approximately 3 mm.

Tracking of tumors to support surgical interventions or radiotherapy planning requires the accurate mapping of every volume position among multiple images series. Deformable organ registration can not be accomplished using image information alone, intrinsic properties of tissue mechanics must also be introduced into the registration process. As level of computational power continues to grow, deformable registration coupled with finite element analysis is becoming a much more accessible tool for medical image applications.

3.2 Correspondence Methods for Registration

The 3-D registration problem can be decomposed into two parts by estimating the point correspondences and the transformation. Since solving for either one without information regarding the other is very difficult, most non-rigid registration approaches use an iterated estimation framework. Given an estimate of the correspondence, the transformation may be estimated which in-turn can be used to update the correspondence. In this Thesis we introduce a, Modified Iterative Closest Point (m-ICP) method, and compare it with two different correspondence methods.

3.2.1 Curvature Scale Space (CSS)

Curvature scale space was first introduced by Mokhtarian and Macworth [96] as a new shape representation for planar curves. The Curvature Scale Space representation is based on the evolution concept - the process of describing a curve at increasing levels of abstractions. The basic idea behind CSS representation is to convolve a parametric representation of the curve with a Gaussian function, as the standard deviation of the Gaussian increases, and to extract the curvature zero-crossing points from the resulting curves.

The curvature of a curve is defined as the derivative of the tangent angle to the curve. Considering the curve in the parametric form $(x(u), y(u))$, where u is an arbitrary parameter, the curvature can be expressed as:

$$k(u) = \frac{\dot{x}(u)\ddot{y}(u) - \ddot{x}(u)\dot{y}(u)}{(\dot{x}(u)^2) + \dot{y}(u)^2)^{\frac{3}{2}}}$$

Special cases of parametrization result in simplification of curvature's formula. If we consider a closed planar curve with normalized arc length parameter $u \in [0, 1]$, the curvature formula will be $k(u) = \dot{x(u)}\ddot{y(u)} - \ddot{x(u)}\dot{y(u)}$. An evolution of the curve can be achieved by Gaussian smoothing to compute the curvature at varying levels of detail. If $g(u, \sigma)$ is a Gaussian kernel of width σ defined by:

$$g(u, \sigma) = \frac{1}{\sigma\sqrt{2\pi}} \exp^{-\frac{u^2}{2\sigma^2}}$$

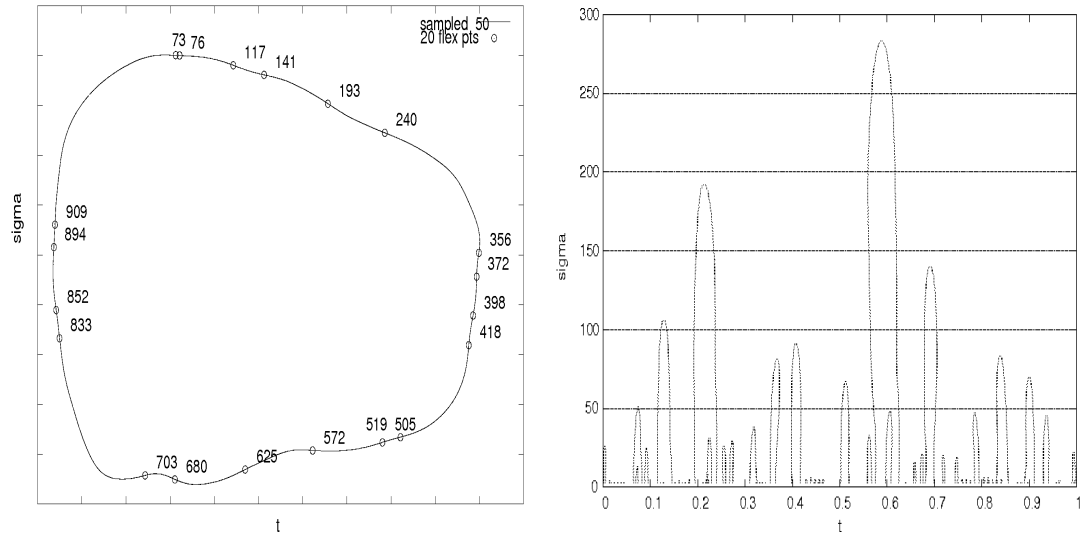

Figure 3.1: Left) At $\sigma = 50$, 20 locations of curvature zero crossing for a planar curve. Right) Curvature scale space image

an evolved curve is defined by $\Gamma_\sigma = \{(X(u,\sigma), Y(u,\sigma)), u \in [0,1]$ where $\otimes$ denotes convolution and:

$$X(u,\sigma) = x(u) \otimes g(u,\sigma)$$

$$Y(u,\sigma) = y(u) \otimes g(u,\sigma)$$

According to the properties of convolution, the derivatives of $X(u,\sigma)$ and $Y(u,\sigma)$ can be easily computed. As σ increases Γ_σ becomes smoother and the number of curvature zero crossing points on it decreases. The binary image called curvature scale space image of a curve is obtained by displaying the resulting points in (u,σ) plane, where u is the normalized arc length and σ is the width of Gaussian kernel. Figure 3.1 shows a curvature scale space image of a planar curve.

Curvature scale space image representation retain the local information of the shape and is robust to noise, scale, and change of orientation.

3.2.2 Modified Iterative Closest Point (deform-ICP)

For most surfaces registration strategies, closest point distances are used as initial estimate of the correspondence. With the presence of deformation, the closest point

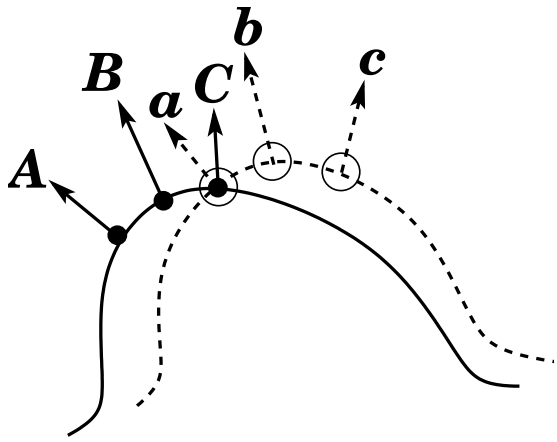

Figure 3.2: Deformable registration process.

operator becomes less reliable as a means for determining correspondence. The classical solution for point registration is the Iterative Closest Point (ICP) algorithm [34] as described in the Chapter IV. The binary point correspondences are based on a nearest neighbor heuristic. The algorithm iterates between the spatial mapping and the nearest neighbor correspondences until the change in the objective error function falls below a preset threshold.

In attempt to overcome the deformation, a modified ICP-like registration based on a local motion function was applied for each point of interest. By implementing the motion function, which allows the points to move along the plane tangent to the surface, the surface shift is better accommodated. Our method augments correspondence functions with surface properties by estimating the non-rigid motion using surface normals. In the standard ICP algorithm, only 3-D point coordinates are used in the estimation of correspondence resulting in a lack of interactions between neighbor points. Instead of assuming a trivial correspondence, the search for the closest points take into account all the neighborhood points with a similar normal direction to the point of interest. The 3-D point coordinates and normals are then put together in a 6-D space and a squared error over the neighborhood around the point of interest is minimized. Figure 3.2 illustrates this approach.

If in the selection of the closest point only the Euclidean distance are used, points a and b from the data set will be associated with point C from the model set. However, the

points a and A from the data and corresponding model set have approximately similar normal directions. In such cases, more weight must be given to the normal component and the proper choice of the closest point is accomplished, $a \rightarrow A$, and $b \rightarrow B$. If we decompose the deformation as a series of small increments, the motion is estimated as a small displacement in the direction of corresponding points. At every increment, the surface of the pre-treatment liver data set is deformed to map on the surface of the post-treatment liver data set, allowing all the points to move in the tangential direction. The main advantage of the algorithm that was developed as part of this Thesis is that the estimation of deformation is accomplished in small incremental steps, and the motion is applied to the corresponding point set at each iteration.

3.2.3 Robust Point Matching (RPM)

Parametric deformable models rely on linear decompositions taken across basis functions and do not, themselves, enforce properties such as one-to-one mapping. To overcome this problem we utilized a Robust Point Matching (RPM) algorithm [100]. The Robust Point Matching (RPM) algorithm was previously developed and used for 2D rigid alignment [97]. The tremendous flexibility of this algorithm was easily generalized to the 2D and 3D affine and piecewise-affine mappings [98, 99]. Furthermore, the algorithm's framework was extended to a general purpose, by including thin-plate spline as the parametrization of the non-rigid mapping and the point-to-point correspondence problem was solved by using a softassign method [98] and deterministic annealing [101]. The main idea of the RPM is to minimize the following fuzzy assignment least squares energy function for the correspondence between point set A, with points $a = \{1, 2..K\}$ and point set I, with points $i = \{1, 2..N\}$:

$$E_{RPM}(M, f) = \sum_{i=1}^{N}\sum_{a=1}^{K} m_{ai}||x_i - f(v_a)||^2 + \lambda||Lf||^2 + T\sum_{i=1}^{N}\sum_{a=1}^{K} m_{ai} log m_{ai} - \zeta\sum_{i=1}^{N}\sum_{a=1}^{K} m_{ai}$$

where m_{ai} are the elements of the fuzzy correspondence matrix M, of point a to point i, with $m_{ai} \in [0, 1]$ and satisfying one-to-one correspondence conditions:

$$\sum_{i=1}^{N+1} m_{ai} = 1 \quad \text{for } i = \{1, 2..N\}$$

$$\sum_{a=1}^{K+1} m_{ai} = 1 \quad \text{for } a = \{1, 2..K)$$

The extra row $N+1$ and extra column $K+1$ are used to handle the outliers. The non-rigid transformation is represented by the mapping function f, a point v_a is mapped to a new location $f(v_a)$. The appropriate constrains on the mapping are introduced by choosing a specific smoothness measure, L, as is reflected in the second term of the energy function. The mapping function is chosen to be a thin plate spline (TPS), and its smoothness is measured in terms of the bending energy within a finite window. The third term is an entropy function with the temperature parameter, T, which controls the fuzziness of correspondence. At higher temperatures, the entropy term forces the correspondence to be more fuzzy. The last term with the weight parameter ζ control the robustness, preventing the rejection of too many points as outliers. The, λ, term is coupled with the temperature, T, in the deterministic annealing process.

The RPM algorithm utilizes an alternating optimization scheme to iteratively updates the correspondence parameter, M, and the spatial transformation function, f, while gradually reducing the temperature, T, which each a function of the other. The spatial mapping is solved in closed form, which permits its use for data of any dimension, 2D or 3D.

3.3 Finite Element Method (FEM): Theory

In the approach presented in this Thesis, deformation of soft tissue is modeled based on the linear elasticity theory. The behavior of an elastically deformable object is governed by a partial differential equations. Finite element methods (FEM) have been regarded as a versatile, effective and accurate technique for discretization of continuum models. In this section, we briefly introduce the linear Finite Element Method for deformable objects.

The total work Π of a deformable elastic system can be written as the sum of the externally applied forces W and the elastic potential energy Λ due to the development of material stresses and strains $\Pi = W + \Lambda$ [66]. In order to determine the object deformation, the material is modeled as a linear elastic continuum in static equilibrium,

with no initial stresses or strains and the total work Π is expanded in terms of the material displacements:

$$W = \int_V F u dV \quad \text{and}$$

$$\Lambda = \frac{1}{2}\int_V \sigma^T \varepsilon dV = \frac{1}{2}\int_V \varepsilon^T D \varepsilon dV$$

where V represents the volume of the deformable object, $u = u(x, y, z)$ is the displacement vector, $F = F(x, y, z)$ is the vector representing all the forces applied, σ is the Cauchy stress tensor and ε is the linear strain tensor. D is the material stiffness matrix relating the stress and strain in Hooke's generalized law:

$$\sigma = D\varepsilon$$

For an isotropic material, the components of the matrix D depend only on two elasticity parameters, Young's Modulus E and Poisson's ratio ν:

$$D = \frac{E}{(1+\nu)(1-2\nu)} \begin{bmatrix} 1-\nu & \nu & \nu & 0 & 0 & 0 \\ \nu & 1-\nu & \nu & 0 & 0 & 0 \\ \nu & \nu & 1-\nu & 0 & 0 & 0 \\ 0 & 0 & 0 & 0.5-\nu & 0 & 0 \\ 0 & 0 & 0 & 0 & 0.5-\nu & 0 \\ 0 & 0 & 0 & 0 & 0 & 0.5-\nu \end{bmatrix}$$

If the continuum object is discretized, it is intended to find an approximation for the equations relating the internal displacements and the external forces applied depending on the material parameters of the model. Four general steps [102] are used in FEM framework :

1. the deformable object has to be discretized into a finite set of elements e, assumed to be interconnected at nodal points on their boundaries. The choice of elements e.g bar (or truss), triangle or tetrahedron, depends on the physical properties of the deformable object under actual loading conditions and how close to the actual behavior the results must be.

2. the displacement functions within each element e has to be defined. Linear, quadratic and cubic polynomials are frequently used function. The displacement functions are often called interpolation functions or shape functions. If n is the number of nodes in the element, the continuous displacement field u of any point inside the element is approximated as a linear combination of the components of the interpolation functions N_i applied to the displacement at the element's nodal points u_i:

$$u_e = \sum_{i}^{n} N_i^e u_i^e$$

Therefore we can express displacement of any point inside of deformable object, from the element node displacements and the element shape functions.

3. strain displacement and stress/strain relationships must be defined. For a elastic object the differences between the original and current positions of all object points are represented by a continuous displacement field $u = [u, v, w]^T$. For small displacements, the relation between the strain ε and the displacement field u is approximated with the linear Cauchy-Green tensor:

$$\begin{bmatrix} \varepsilon_x \\ \varepsilon_y \\ \varepsilon_z \\ \gamma_{xy} \\ \gamma_{yz} \\ \gamma_{zx} \end{bmatrix} = \begin{bmatrix} \frac{\delta u}{\delta x} \\ \frac{\delta v}{\delta y} \\ \frac{\delta w}{\delta z} \\ \frac{\delta u}{\delta y} + \frac{\delta v}{\delta x} \\ \frac{\delta v}{\delta z} + \frac{\delta w}{\delta y} \\ \frac{\delta w}{\delta x} + \frac{\delta u}{\delta z} \end{bmatrix}$$

Using nodal displacements u_i of point i in x-y-z directions the strain displacement is defined as: $\varepsilon = B_e u$ where

$$B_e = \begin{bmatrix} \frac{\delta}{\delta x} & 0 & 0 \\ 0 & \frac{\delta}{\delta y} & 0 \\ 0 & 0 & \frac{\delta}{\delta z} \\ \frac{\delta}{\delta y} & \frac{\delta}{\delta x} & 0 \\ \frac{\delta}{\delta z} & 0 & \frac{\delta}{\delta x} \\ 0 & \frac{\delta}{\delta z} & \frac{\delta}{\delta y} \end{bmatrix}$$

4. derive the element stiffness matrix and equations . An equilibrium expression is derived for each element e and then assembled in a large and sparse linear system. The relation between the nodal forces f_i and the nodal displacements u_i which has to be minimized at every node i of each element e, assuming that point loads are acting on the nodes, can be expressed as :

$$\prod = \frac{1}{2}\int_V \sigma^T \varepsilon dV - \sum_i u_i^e f_i^e$$

In the linear finite element formulation became:

$$\prod = \frac{1}{2} u_e^T K_e u_e - \sum_i u_i^e f_i^e$$

with

$$K_e = B_e^T D B_e V_e$$

K_e is the element stiffness matrix and V_e volume of element. Equilibrium corresponds to a minimum of Π. To determine the extreme values, the partial derivative of Π are solved with respect to nodal displacements u_i and the relation between displacement vector u and the force vector f is obtained for each element:

$$K_e u_e - f_e = 0$$

The only remaining step is to assemble the global stiffness from the element stiffness matrices. The result is a large and sparse linear system, the solution of which will provide the deformation field corresponding to the global minimum of the total work:

$$F = Ku$$

where K is the stiffness matrix numerically integrated over the object´s volume, u is a displacement vector of all nodes and F is a vector that combines all external forces and boundary conditions which describe the initial and the end states of the deformation process. The dimension of global stiffness matrix K is $3Nx3N$ and the dimension of the global force vector F is $3N$ where N is the total number of nodes.

Hence, this method is one in which a continuous quantity, such as the displacement throughout the body, is approximated by a discrete model composed of a set of piecewise-continuous functions defined within each finite element. The precision of the approximation improves with the level of discretization, and the degree of interpolation chosen, but to the detriment of computational time and memory size. A number of advantages that include the ability to: (1) model objects composed of several different materials because the element equations are evaluated individually; (2) vary the size of elements where necessary; (3) manage unlimited number of boundary conditions; and (4) manage nonlinear behavior existing with large deformations and nonlinear materials. All of these features have made the FEM very popular in the area of deformable models and surgical simulations.

3.4 Tumor Tracking Model

We present a surface based non-rigid method for tracking tumor across pre- and post-treatment CT liver images using a finite element model based deformable system. The strategy of the algorithm is twofold: the first step is to align the liver's mesh surfaces and the second step is to model the volumetric deformation using a linearly elastic finite element model (FEM) which has boundary conditions generated from the result of surface registration. When the liver is treated as a purely elastic body, at the equilibrium state, the strain energy stored as tissue distortion is equivalent to the work of external forces applied to its surface. In this framework the major challenge for tracking tumor location is not the tissue mechanical properties for FEM modeling but the evaluation of boundary conditions defined by the correspondence of liver boundary points on 3D image sets taken at different times. Different registration algorithms, presented in Section II, have been investigated to determine the proper correspondence of the boundary points which ultimately drive the transformation. To accommodate the local deformation, the problem of tracking tumor location can be formulated as the bijective relation of recovering location of any points from the pre-treatment images in the post-treatment image.

In this formulation, surface/volumetric based registration-deformation algorithm can

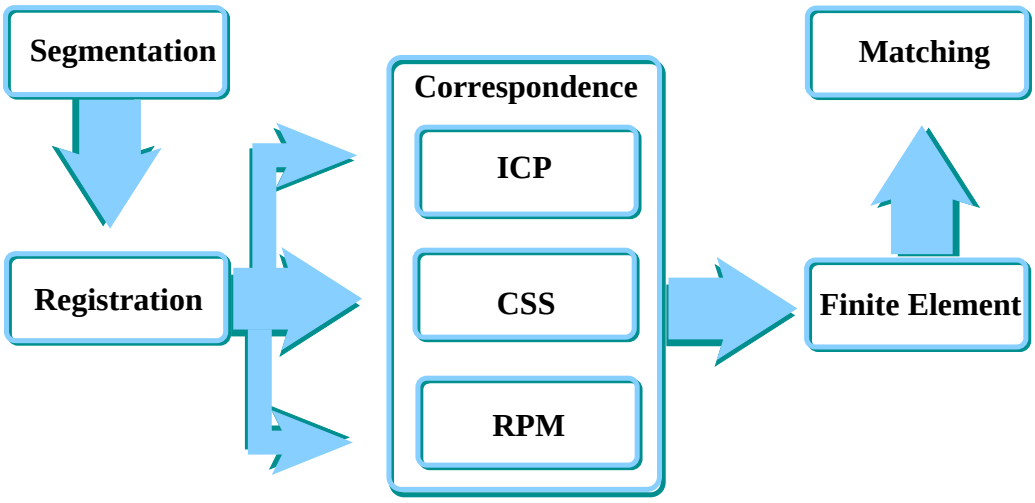

Figure 3.3: Flow chart of the integrated process to quantify tumor motion

be decomposed into three main components: extracting boundary points of interesting structures from images, matching the data and model surfaces, and then extending the surface-based transformation to the full volume using FEM. Figure 3.3 describes the main steps of our approach.

3.4.1 Segmentation and 3D Mesh Generation

Two data sets of tomographic images were acquired using GE Light Speed VCT scanner. The pre-treatment CT scan was taken at normal exhale and inhale breath-hold and the post-treatment contrast was acquired at inhale. Contrast enhanced images provide detail allowing accurate definition of the margins for both liver and tumor. The data set consists of axial slices of 1.25 mm thickness and matrix size of 512 x 512 pixels of the entire body. The fist step in mesh generation is to extract the liver and tumor's contour shapes from these data sets. Segmentation process generate a series of discrete contours which are represented by a list of vertexes associated with each transversely image slices. The contour extraction was performed using MIPAV software package [103] using a two dimensional semi-automated active control model. The segmented contours were converted to a volumetric binary mask. The data set for the liver was reduced to approximately 180 slices and while the tumor data set is patient specific, varying between 30-40 slices. The binary mask was converted to a tri-element surface mesh using the

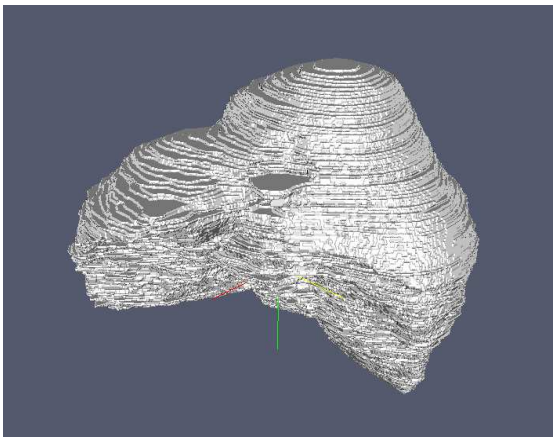

Figure 3.4: Result of the original surface with Marching-cubes algorithm

sub-voxel triangulation marching cubes algorithm [104]. The basic principle behind the marching cubes algorithm is to subdivide the data space into a series of small cubes on a voxel-by-voxel basis. The algorithm 'marches' through each of the cubes testing the intersection of the 3D contour surface with each voxel and replacing the cube with an appropriate set of polygons. The total sum of all polygons generated will be further reduced to a triangle surface representation called mesh, that approximates the one the data set describes. The result of marching cubes algorithm on liver surface mesh is shown in Figure 3.4.

However, the resulting polygonal surfaces were too rough and the number of triangles generated too large for further processing. Using Visualization Toolkit [105], smoothing and decimation algorithms were developed in order to avoid staircase effects and to simplify the mesh. The mesh was smoothed using a windowed sinc function interpolation kernel [106]. The basic idea of Taubin group [106] design was to approximate the transfer functions of the low-pass filters by Chebyshev polynomials using standard signal processing low-pass filters. As opposed to kernel convolution, using Chebyshev polynomials made possible to apply the filters in an iterative diffusion process. The more smoothing iterations applied, the higher the degree of polynomial approximating the low-pass filter transfer function. Each smoothing iteration, therefore, applies the next higher term of the Chebyshev filter approximation to the polyhedron. This decoupling of the filter into an iteratively applied polynomial is possible since the Chebyshev

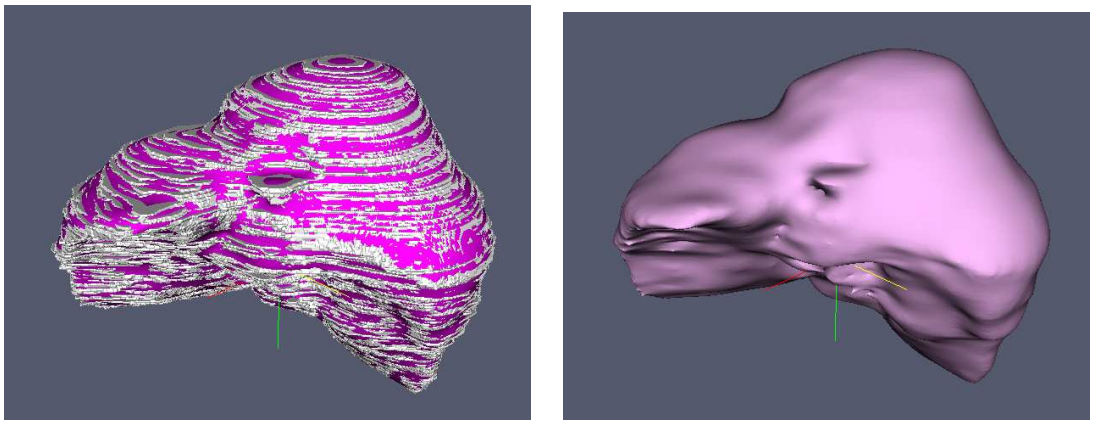

Figure 3.5: Windowed sinc smoothing result : Left) The smoothed mesh superimposed with the original one. Right) Smoothed mesh

polynomials are orthogonal, i.e. increasing the order of the approximation to the filter transfer function does not alter the previously calculated coefficients for the low order terms [105]. The meshes for liver, were smoothed in 100 iterations with pass band value for the windowed sinc filter of 0.001. The tumors were smoothed with fewer iterations to maintain the surface irregularities. An example of the smoothing process for the liver is illustrated in the Figure 3.5.

The number of triangles in the mesh was reduced by applying a quadric decimation filter [107] allowing fast and accurate geometric simplification of the mesh. This approach defines for each face of the mesh a quadric equal to the squared distance of a point to the plane containing the face. For each vertex in the mesh is assigned the sum of quadrics on its adjacent faces weighted by the face area. After the decimation process is complete less storage space is required while maintaining an accurate description of volume. The meshes were reduced down to 10% of their original size. The combined effect of the smoothing and the decimation algorithms was to adjust the triangles of the mesh, making them more evenly distributed, improving the appearance while maintaining accurate mesh topology. An example of the process of generating a liver surface mesh is shown in the Figure 3.6.

Based on the simplified triangulation of the surface, the volume of liver with the tumor embedded was decomposed into tetrahedral elements without changing the surface topology. The goal was to generate suitable tetrahedral meshes for numerical simulation

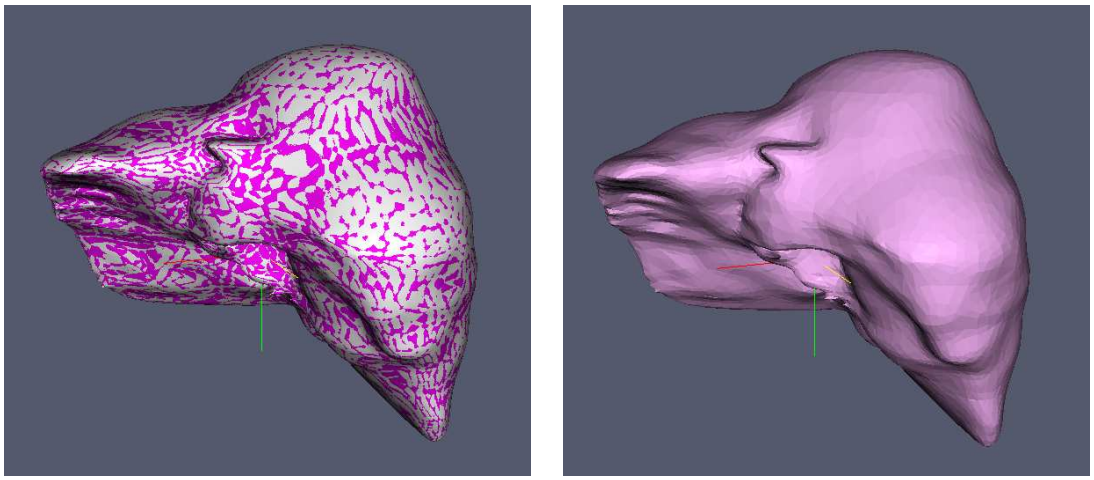

Figure 3.6: Quadratic filter decimation: Left) The smoothed mesh superimposed with the decimated one. Right) Decimated mesh

using finite element. We have chosen this element because a tetrahedron does not self-penetrate, whereas a higher order element tends to deform and result in self-intersection.

We used a public domain quality tetrahedral mesh generator TetGen [108], which is based on an implementation of Constrained Delaunay algorithm [109]. A constrained tetrahedralization is a decomposition of a three-dimensional domain into a tetrahedral mesh, such that the output boundary is enforced to the input boundary represented by the faces of the mesh. This feature proved to be very useful, in our case for combining two meshes which share the same boundary, furthermore the boundary surfaces of the objects represented in the mesh can be extracted from the mesh as triangulated surfaces. In FEM numerical simulation, the mesh shape and mesh size are important for the approximation error and convergence of the numerical methods. TetGen performs efficient mesh refinement, inserting new vertexes, to improve the overall mesh quality. For accuracy in the FEM it is necessary that the shapes of the elements have a small radius-edge ratio and a maximum volume element constraint. The radius-edge ratio of an element is the ratio of the radius of the unique circumsphere to the length of the shortest edge. The resulting tetrahedral mesh is a finite element mesh which consists of good-shaped tetrahedrons and the mesh size well conforms to the boundary size - the mesh size is small close to the boundary and is gradually increased to the interior.

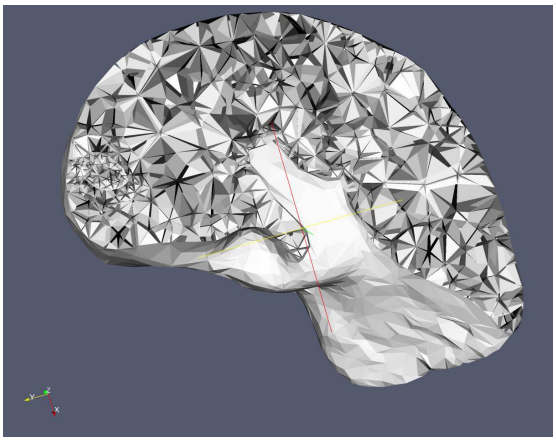

Figure 3.7: A fully connected and consistent tetrahedral mesh for liver and tumor.

The following figure 3.7 illustrate a fully connected tetrahedral mesh containing both the liver and the tumor.

3.4.2 Boundary Conditions from Registration

Figure 3.8 left shows the result of the ICP registration algorithm. Because of the nonlinear/deformation motion of the liver between consecutive studies, accurate surface registration can not be obtained when only rigid registration algorithms are used. Figure 3.8 right shows an example, where the tumor associated with the pre-treatment liver was erroneously registered out of surface of the post-treatment liver because of the noted limitations of such algorithms.

Our approach starts with a rigid registration step necessary to provide the best alignment of the pre-treatment/data and the post-treatment/model surface meshes followed by the deform-ICP registration method previously described. The liver's external surfaces are registered based on the change in surface positions leaving the deformation of the interior volume as the residual error to be accounted for by the finite element analysis. The FEM will compute the deformation of the tumor's surrounding nodes in the mesh. This combination of the registration which provide the boundary conditions assigned to surface nodes and the finite element modeling which is used to infer tumor location in subsequent studies has proven to be extremely reliable during the course of

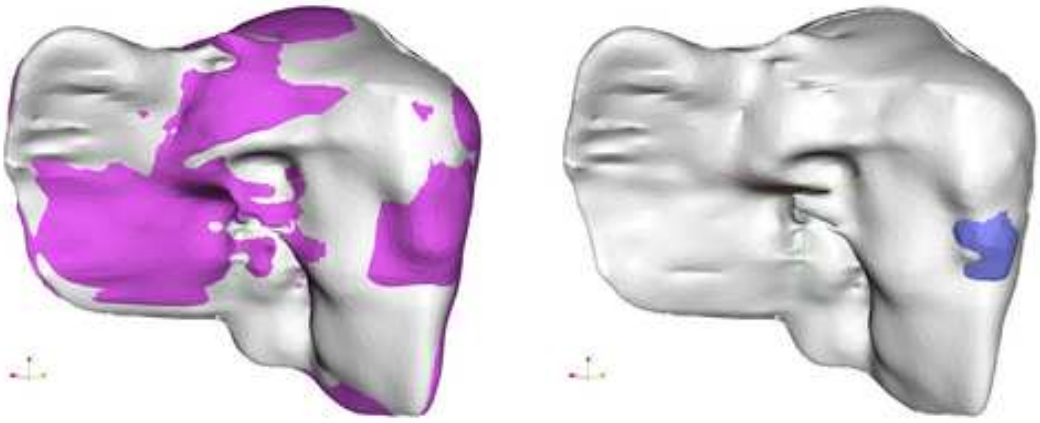

Figure 3.8: Left) Result of rigid ICP registration: light colored surface shows the post-treatment, and dark colored is the liver pre-treatment. Right) Rigid registration technique do not correct for the surface deformation: post-treatment (light color) and pre-treatment tumor.

our experiments.

3.4.3 Finite Element Implementation

Once the image sets are registered, the final step of our approach is to model the deformation based on the linear elasticity theory. Accurate prediction of tumor location rely on accurate representation of soft tissue. We assume that liver tissue is an elastic, incompressible material (no volume change during deformation), isotropic (no directional preference) and homogeneous (same tissue composition). Given an elastic object represented as volumetric mesh, deformation induces the movement of every vertex within the object. This can be modeled as a mapping function of the positions of all vertices from the initial configuration to those in the deformed configuration.

We take advantage of the tetrahedral volumetric mesh building in this structure our finite element model with a 2-node element. Our resulting mesh structure is a consistent tetrahedral mesh that contains physically connected liver and tumor. We have chosen this 2-node element because:

- each node has a relatively small number of neighbors resulting in fewer non-zero elements in the stiffness matrix and less expensive computation.
- it simplifies the integration of the derivatives of the potential energy.

Instead of using forces, which are difficult to determine accurately, we impose boundary conditions to the liver object by assigning fixed values to the displacement vector, u. Boundary conditions are assigned to surface nodes based on the change in node positions during registration. Material properties and these boundary conditions which are integrated over each element of the mesh and distributed over the mesh's nodes drive the deformation and the deformation propagates throughout the entire volume. Free software package Z88 [110] was used to generate the solution of the linear system of equations by a preconditioned conjugated gradient method. The solution of the linear system provide the displacements of all internal nodes of the volumetric mesh, allowing reliable tracking of each tumor's deformation.

3.5 Phantom Validation of Deformable Registration

Quantitative validation of the deformable registration algorithm has proved to be difficult because of the general lack of ground truth information. Since there is rarely if ever a "gold standard" with which to evaluate nonrigid registration results, semi-quantitative evaluation by a human expert is often used as a substitute. To test the performance of the algorithms we designed and evaluated both 2-D synthetic data and imaged beef liver containing phantoms to address this issue. Comparative performance analysis was conducted using both rigid and non-rigid approaches.

The basic idea comes from the fact that for an elastic object, the strain energy of the object equals the work done by the external forces applied. The effect of the material parameters is limited if all the displacements are prescribed from the results of registration.

3.5.1 2D Rubber Phantom

We have created a rubber balloon model that can be used to induce measurable deformations. The balloon was stretched over a circular ring with the diameter of 42 mm. A closed curve was drawn on the balloon in the shape of a 2-D liver section and 21 points of 1 mm diameter were drawn inside the closed curve with uniform distribution.

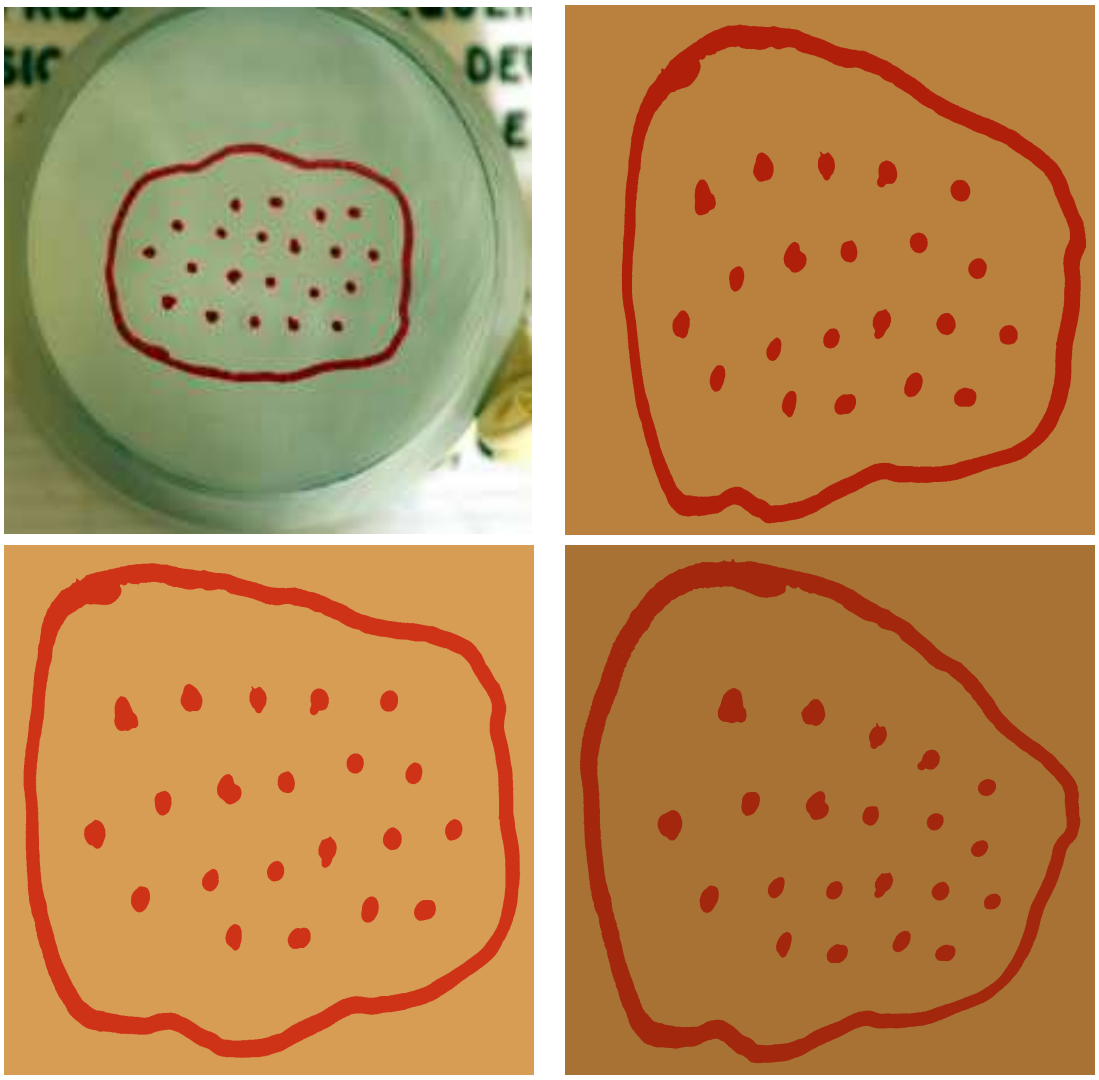

Figure 3.9: The base 2D rubber phantom model and three deformation representation.

The centroids of these points served as targets while performing multiple deformations of the curve to simulate consecutive visits. In all, the base model was deformed into three different representations that were generated by manually stretching the balloon at different locations. Figure 3.9 displays the balloon base model and the three deformed states.

The four-step algorithm previously presented was evaluated in order to predict the location of the markers in all deformed data sets. Using the open source software Auto-Trace [112] the contours of the closed curve and the 21 marked points were automatically segmented from all four representations. A one-to-one correspondence was assigned for

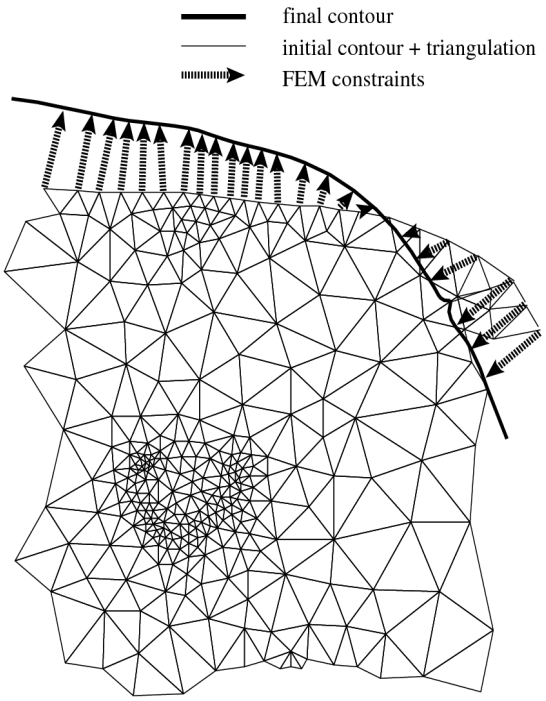

Figure 3.10: Boundary conditions and finite element triangulation.

the markers in all deformed states. In order to evaluate the proper correspondence in the applied boundary conditions, the closed curves were registered using three different algorithms: CSS, deform-ICP, RPM. The next step of our approach was to model deformation using the finite element method. The interior of the closed curve with all 21 markers were tessellated using the two-dimensional finite element mesh generator and Delaunay triangulator, Triangle [113, 114]. The following Figure 3.10 illustrates the two steps procedure: registration followed by the finite element analysis.

The degree of deformation of the 2D rubber phantom was characterized as the length of the displacement vectors of all $i = 1..21$ markers. The centroid locations of the destination markers in the image are c^i_{dest}. When we register based on rigid-ICP, the centroid locations of the markers are $c^i_{rigid-ICP}$ and after applying our deformable surface registration model, the centroid locations of the markers in the deformed image are c^i_{deform}. Therefore the accuracy of the deformation model can be quantitatively calculated by the vector length:

$$d_i = \parallel c^i_{dest} - c^i_{deform} \parallel$$

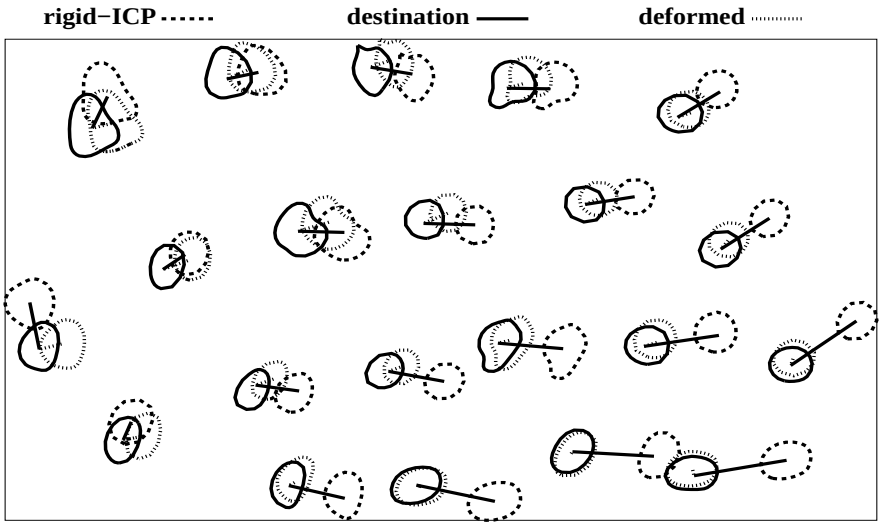

Figure 3.11: 2D phantom evaluation of the displacement vector of the markers: the Euclidean distance between the result of deformation and the destination state is computed.

Figure3.11 graphically illustrates the results of deformation from our FEM model superimposed with the destination image. Different amounts of deformation can be experienced in different regions due to the smaller concentration of deformations in the central regions and the larger amount at the periphery areas. Figure 3.11 shows that the deformations exhibit a greater effect on peripheral markers as compared to central ones.

We have four instances of deformation data sets and twelve registration-deformation results are obtained, generating a distribution of displacement vectors. The minimum, average and maximum of displacement for all markers over all twelve results are shown in the Figure 3.12 and the mean value is reported in the table.

The average error for the registration achieved using a finite element model was slightly higher when deform-ICP algorithm was used (1 mm), than with Robust Point Matching (RPM) algorithm (0.7 mm). This error may be due to the lack of correspondence information provided in the calculation of the boundary conditions.

In order to further improve results we studied the manner in which radiologist have traditionally assessed consecutive imaging studies. Radiologists typically look for blood

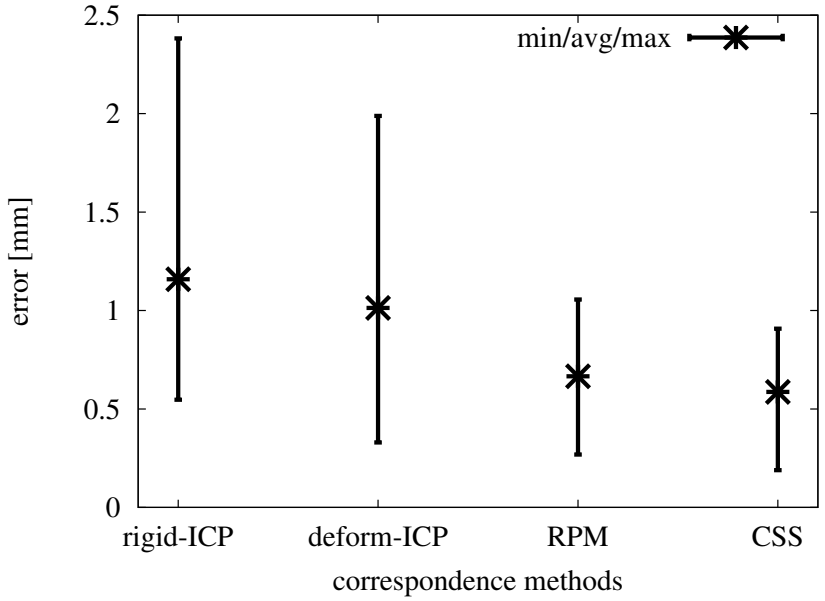

Displacement of markers [mm]

	Mean	Max
rigid-ICP	1.2	2.4
deform-ICP	1	2
RPM	0.7	1.1
CSS	0.6	0.9

Figure 3.12: 2D registration errors for different correspondence methods: deform-ICP, RPM and CSS algorithms.

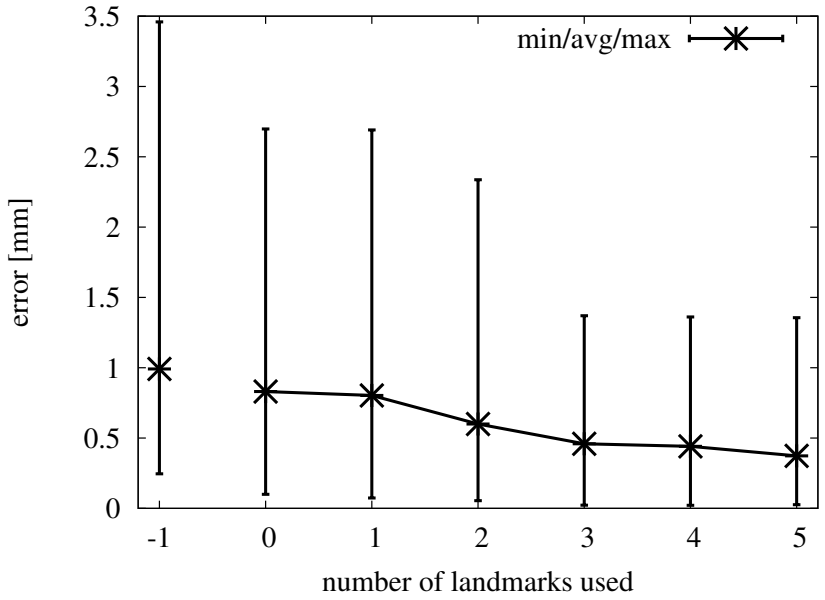

Figure 3.13: Deform-ICP registration errors with different number of landmark points.

vessels landmarks, but in trying to implement an analogous procedure using a computer-based approach the difficulties arose while extracting landmarks in the two images that actually correspond to the same physical point. To evaluate the potential of this approach we have randomly chosen a small number of representative landmark points in the original, undeformed image and specifically track each of them in the deformed images. This approach was efficiently implemented by including the landmark points in the further deformation surface registration processing and analysis. To avoid any simulation inconsistencies, the landmark points were chosen in the central zone of the image and we force them to be part of the FEM node structure. Using deform-ICP algorithm the deformation results when different number of landmark points are used are presented in the Figure 3.13. The average registration-deformation error is about 0.5 mm when 3 landmark points are used, with maximum error between 0.7 mm and 0.3 mm when 1 respectively 5 landmark points are used.

A motivation for using this particular solution is that it can be easily introduced into the existing work flow of radiologist. By having the radiologist induce a few landmark points the accuracy is improved while at the same time the computer-assisted tools add speed and reliability to the radiologist´s assessment, helping them in the interventional

and treatment planning process.

3.5.2 3D Beef Liver Phantom

The accuracy of the deformable model was evaluated using a real beef liver. To simulate the internal abdominal environment and to minimize assumptions, the beef liver was embedded in an agar gel to preserve the natural shape. Using a syringe 21 plastic beads were uniformly distributed throughout the liver. All the markers had the same spherical shape with diameter of 5 mm. To enable accurate segmentation and position estimation, the diameter of the spheres were chosen to be slightly larger than the distance between two successive scanning planes. For our purposes Z spacing was 1 mm. The plastic markers were easily identified in all of the CT scans without creating any noticeable imaging artifacts. The markers are well suited to validate our model. The liver was imaged, deformed and re-imaged to simulate changes in shape of the liver that can occur due to differences in patient position across consecutive imaging studies. The markers do not exhibit shape variations as can occur in actual tumors which have been partially ablated.

The deformable registration component of our approach is based on changes in surface position, thus three deformation types characteristic for real patient acquisitions were simulated by compressing and tilting the container with the beef liver. The beef liver phantom data sets were scanned with General Electric LightSpeed CT scanner. Volumetric images were obtained using the following scanner settings: 120 kV, 180 mA, standard reconstruction type, and high quality scan mode. The field of view was 230 mm, producing a voxel size of 0.45 mm x 0.45 mm x 1mm. Each CT scan was composed of 130 slices of 1 mm thick (512 x 512 pixels, 16 bits) exported in DICOM format. Figure 3.14 displays the original setup of the beef liver and to illustrate the deformation data sets that were generated we include two CT sections targeting the same marker.

Using the open source software MIPAV [103] the 3D surfaces of the beef liver and all markers were semi-automatically generated from the DICOM files for all four representations. A one-to-one correspondence was assigned for the markers in all deformed states. Figure 3.15 shows all the markers uniformly distributed in the liver.

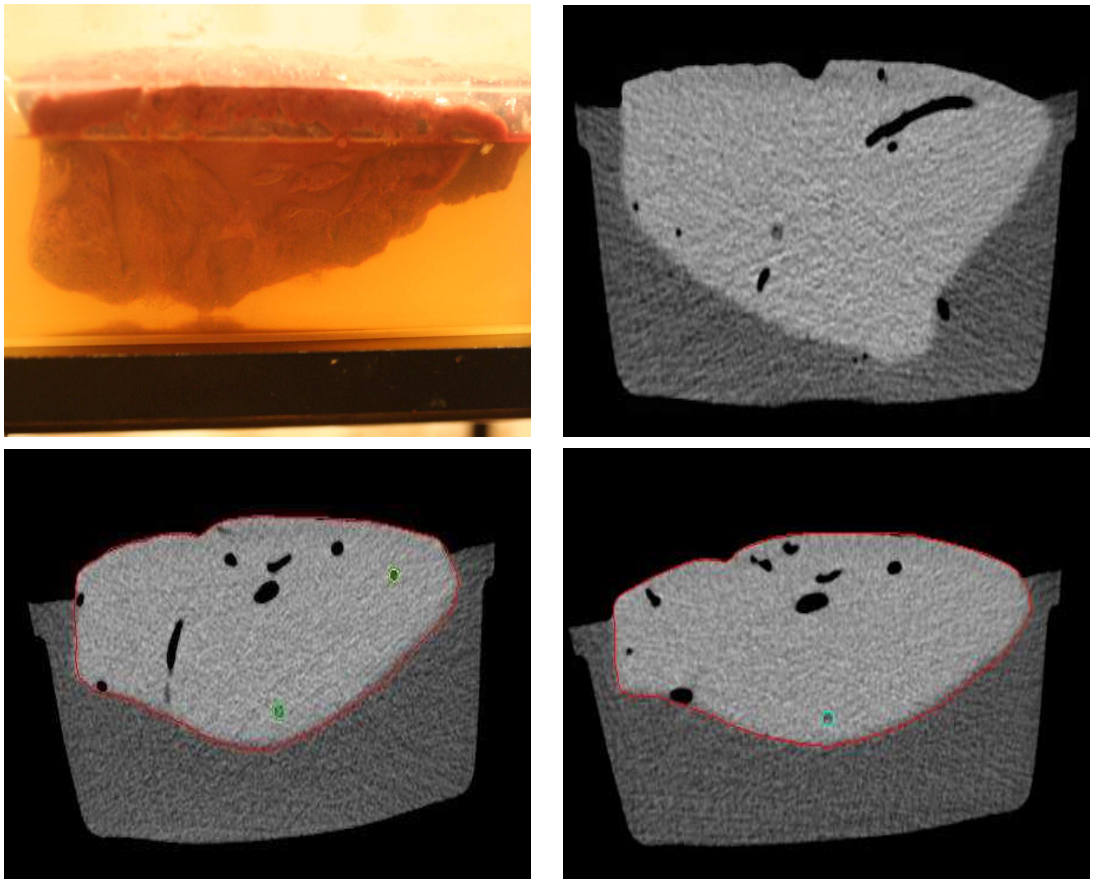

Figure 3.14: 3D beef liver phantom: Upper row) initial setup with a CT section. Lower row) CT section of two deformation data sets, targeting the same plastic bead marker.

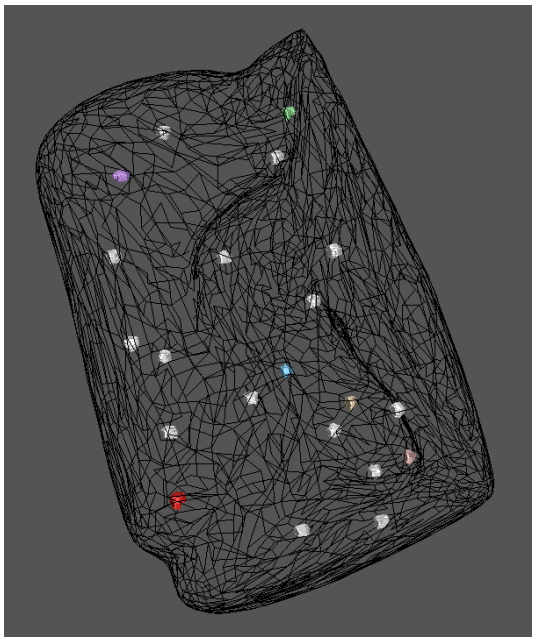

Figure 3.15: 3D markers uniformly distributed inside the beef liver.

Data Sets	Surface mesh				Volumetric mesh		
	Marching cubes		Smoothing & Decimation				
	Points	Facets	Points	Facets	Points	Facets	Tetrahedrons
Original	270200	540000	2723	5401	3856	35412	16356
Deformation 1	238400	476400	2405	4765	3372	31098	14358
Deformation 2	221800	443200	2239	4433	3196	29618	13701
Deformation 3	238900	477400	2410	4775	3457	32103	14858

Table 3.2: Number of points generated in the construction of liver surface and tetrahedral volumetric meshes.

Using the three-dimensional mesh generator TetGen [108], a high quality tetrahedral meshes were created that conform to the input surface meshes, so that some nodes of this model corresponded to the centroids of the markers. Table 3.2 summarizes the number of points generated for liver surfaces and for the tetrahedral volumetric meshes.

In this tetrahedral mesh structure we built a finite element model with 2-node element, so that the markers share common mesh nodes with the liver, allowing the volumetric displacements of the markers to be inferred from liver's surface deformations using FEM. As mentioned in the previous section the displacement of all vertices in the volumetric mesh can be reconstructed by the linear force-deformation relation $Ku = F$, for a stiffness matrix K with parameters Young's modulus E and Poisson's ratio ν. The liver is filled with blood, which implies that ex vivo tissues should not behave like in vivo tissues. The elastic properties of the liver have shown a strong variability. Appropriate linear elastic material parameter values for the beef liver were determined from literature [111]. Most soft tissues are considered as roughly incompressible materials and are assumed to have a Poisson's ration in the range of $0.45 < \nu < 0.49$. We assume the model material properties as isotropic and linear with E describing the stiffness of the material of 11 kPa and ν describing the compressibility of the material of 0.47. Only the Poisson's ratio is important in our FEM analysis since only displacement boundary

Marker	Rigid ICP	Deform ICP	RPM
1 - peripheral	12.9683	6.6741	1.49918
2 - peripheral	11.5913	3.94894	2.41309
3 - peripheral	16.9037	8.70856	1.1506
4 - peripheral	8.09239	5.82661	3.15514
5 - central	7.99102	2.67276	0.81779
6 - central	7.65066	2.85603	2.43957
7 - central	6.35848	4.72732	1.75357

Table 3.3: Improvement of markers error [mm] as a result of finite element modeling

conditions were applied. Free software package Z88 [110] was used to generate the solution of the linear system of equations by a preconditioned conjugate gradient method. The finite element analysis was performed in a single step on a Centrino Duo 1GHz Dell with 1GB of RAM and the average clock time was 10 seconds.

The accuracy of the deformation depend on the deviation of the displacements and the boundary conditions generated by the surface registration. In order to evaluate the proper correspondence in the applied boundary conditions, the livers surfaces were registered using deform-ICP and Robust Point Matching algorithms. The displacement values of deformation for some central and peripheral markers are shown in the Table.

There were four instances of the deformation data sets and twelve registration-deformation results were obtained, generating a distribution of displacement vectors. The minimum, average and maximum of displacement for all markers over all twelve results are shown in the Figure 3.16 and the mean value is reported in the table.

The FEM model provides significant improvement over results from rigid registration alone. Since the model is primarily driven by the surface data, the method by which boundary conditions are chosen for each node can play a significant role in the resulting accuracy. The maximum registration error when the deform-ICP algorithm was used was - 9 mm and at the cost of greater pre processing time was 5 mm when Robust Point Matching (RPM) algorithm was used.

The potential sources of errors can occur from:

- segmentation - surface based registration algorithms suffers from surface segmentation errors.

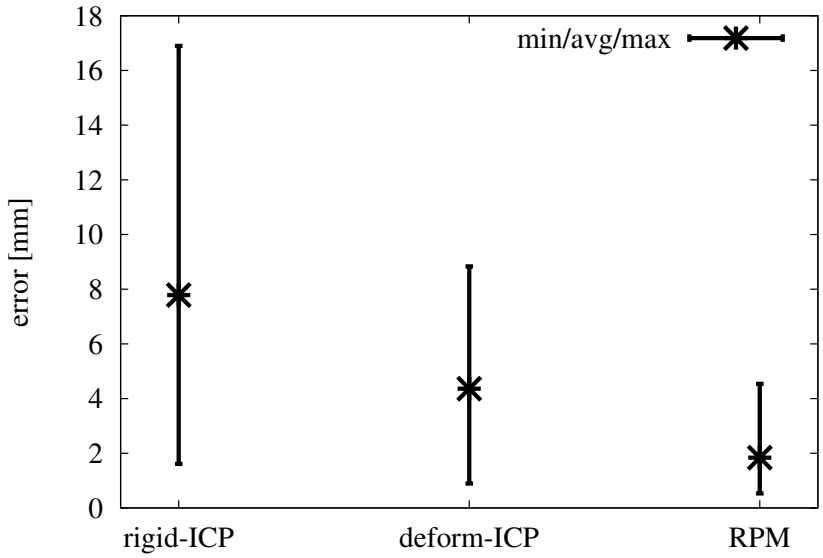

Displacement of markers [mm]

	Mean	Max
rigid-ICP	8	17
deform-ICP	4	9
RPM	2	5

Figure 3.16: 3D registration errors for different correspondence methods: deform-ICP and RPM.

- finite element modeling - discretization errors resulted from geometric differences between the boundaries of the model and its finite element approximation, and modeling errors due to numerical integration in solving the linear system.

- material properties measurements - the same average values of experimentally derived material properties for both liver and tumors are used in our finite element analysis. Once again, since boundary conditions are used to drive the deformation, the accuracy involved in the material properties is not as important as the accuracy involved in approximating the shape of the livers in the model.

We did not take in account the possible migration of the implanted markers, but the obtained mean displacement errors of deformation demonstrates very good results and is in agreement with previous studies done for these cases. The registration accuracy and possible migration of internal fiducial 2 mm gold markers implanted into 4 patients with liver tumors and 14 patients with prostate cancer were investigated by Kitamura et al. [115]. Using a real-time tumor-tracking radiation therapy system, the relative relationship between the coordinates of the center of mass of the organs and those of the markers were calculated. Assuming that organs do not shrink, grow, or rotate the maximum standard deviation of migration error in each direction was estimated to be less than 2.5 mm for the liver and less than 2.0 mm for the prostate.

3.6 Patients Study

The proposed model for deformable liver surface registration was used to predict the location of the tumors in data sets corresponding to three patients with liver metastases which have one hepatocellular carcinoma. Before treatment planning each patient underwent to an intravenous contrast CT imaging. The liver was imaged during breath-hold (reducing respiratory motion artifacts) before and after the injection of contrast during selected phases of contrast distribution, (typically early and late hepatic arterial phase and portal venous phase). All images used in our model were acquired during the portal venous phase because the important details for detecting and characterizing hypo vascular lesions and metastatic deposits are apparent during this phase. At the

time of radio-frequency ablation treatment another CT scan of the patient was obtained in the exhale breath-hold position. A diagnostic contrast inhale CT scan was obtained 1, 3 and 12 months after the completion of treatment. Volumetric images were obtained with General Electric LightSpeed CT scanner, using the following scanner settings: 120 kV, 180 mA, standard reconstruction type, and high quality scan mode. The resolution of the CT was 512 x 512 x n, where n varied to accommodate the patient extent and the voxel size was 0.93 mm x 0.93 mm x 1.25 mm slightly varying between patients. Figure 3.17 shows the pre-treatment, 1 and 3 month follow-us CT scan and for the patients.

The tumor location is determined by visual comparison of the predicted and actual positions as shown in the Figure 3.18.

Kitamura et al. [116] implanted a 2 mm gold marker near tumors to investigate the impact of tumor location, cirrhosis and history of liver surgery on the motion of tumors throughout the liver in the trans axial direction. They reported the average amplitude of tumor motion in the 20 patients was 4±4 mm (range, 1-12 mm) in the right-left direction, 9±5 mm (range, 2-19 mm) in the craniocaudal direction, and 5±3 mm (range, 2-12 mm) in the anteroposterior direction.

In general, rigid registration of the segmented liver reasonably aligned the central area of the organ, while the residual deformation, relatively larger in the periphery, was evaluated by the FEM model. The liver deformation using linear elastic model gradually deepens with an increasing force load. To demonstrate the potential of the proposed model we have applied it to test non-rigid registration of portal vein. We assume the CT data from 1 month follow-up as visit 1 and 3 month follow-up as visit 2. Because of the ramification of the shape of the portal vein it was broken into three regions, left, middle and right. Each of which was used as virtual tumor targets, as shown in the Figure 3.19.

The boundary conditions were applied, while holding the central parts of the liver in fixed position and forcing displacements in the other regions that as dictated by their distances resulted from deform-ICP algorithm. The registration deformation errors were evaluated for portal vein by using root mean square residual error between the two targets. This metric used in the minimization process of ICP registration algorithm

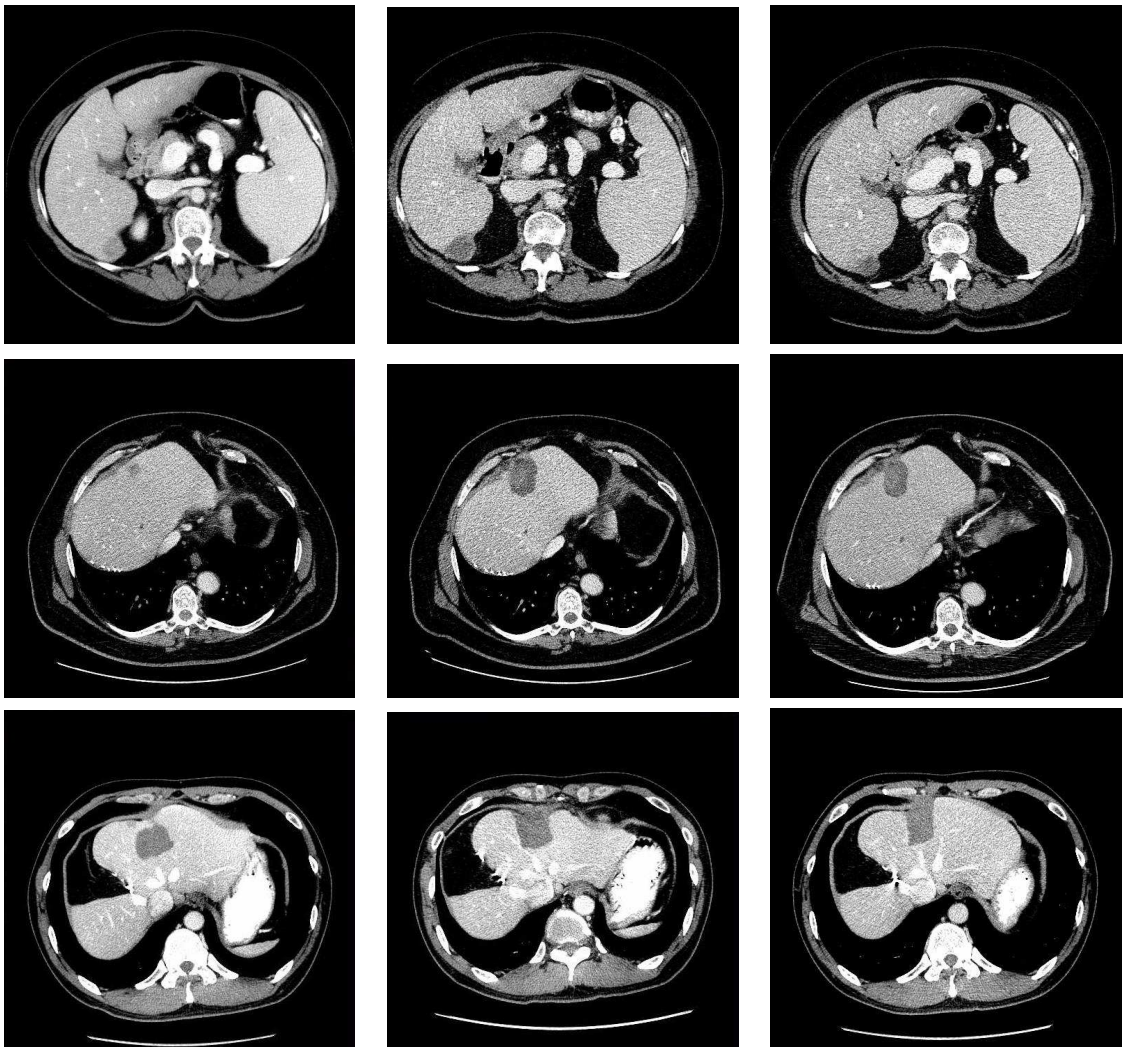

Figure 3.17: CT scans for three patients treated by per-cutaneous radiofrequency ablation of HCC : the first column the pre-treatment images, the second column 1 month follow-up, and the third column 3 months follow-up. The last patient was re-evaluated for suspected relapse, thus the pre-treatment image is considered after the first RFA.

Figure 3.18: Visual comparison of tumor location.

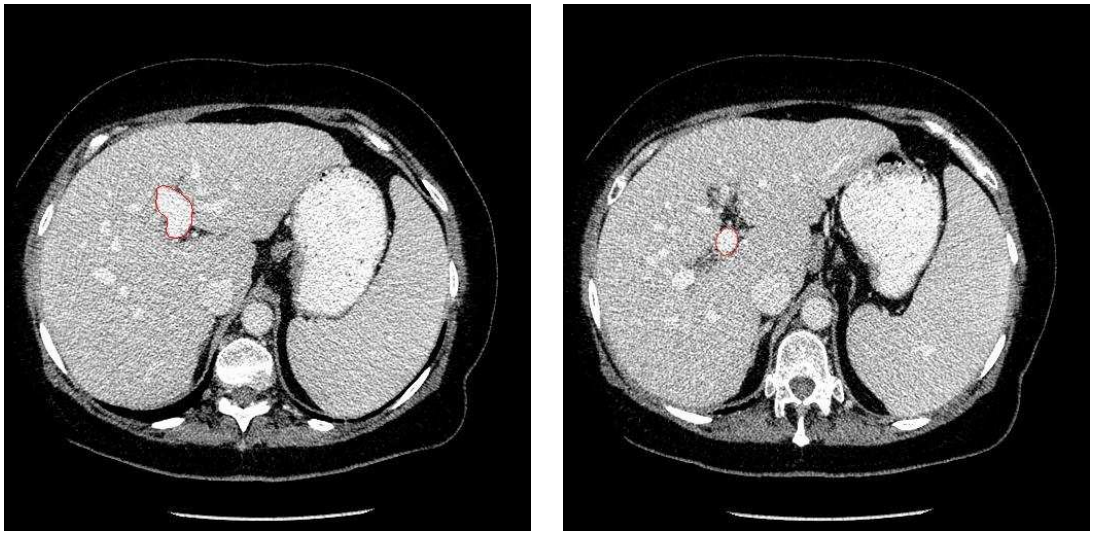

Figure 3.19: Left portal vein and middle portal vein.

describe the total error of fit between the two surfaces. The two meshes are compared by calculating the mean and standard deviation of the distances between the deformed surface from visit 1 and the original data from visit 2. The quantitative analysis results for left and middle portal vein data are shown in the Figure 3.20.

Figure 3.21 shows the result of deformation when both portal vein and the tumor are integrated in the model.

3.7 Summary

Patient follow-up studies which can reliable correlate the spatial position of tumor recurrences and progression are very important in interventional procedures. In order to accurately simulate soft-tissue changes, physically motivated deformable models are required and the parameters of the tissue must be well defined. While is a challenging problem to obtain realistic material properties, such as Young's modulus and Poisson ratios, for all the tissues and structures that constitute the liver, we were able to design, develop and evaluate a reliable and efficient method for predicting changes in tumor location across pre- and post-treatment with radiofrequency ablation using simple approximations. The method incorporates a non-rigid registration and a linearly elastic finite element model. Surface matching between pre- and post-treatment data was performed by the modified ICP algorithm and the results were input as boundary conditions for the finite element model to calculate the volumetric deformation. We demonstrated the convergence and robustness of this approach using both phantom data and actual patient data sets.

Deformable surface registration is obviously a sine qua non for interventional radiology. Careful planning of RFA interventions is of great importance in order to limit the damage of the healthy tissues. The results of the deformable registration model can be easily integrated in the scan reading work flow performed by physicians. Using the current standard of care for CT screening this procedure is performed without the benefit and guidance of intravenous contrast. Under these conditions it is possible to identify the liver, but the tumor margins are often not visible. Through deformable registration,

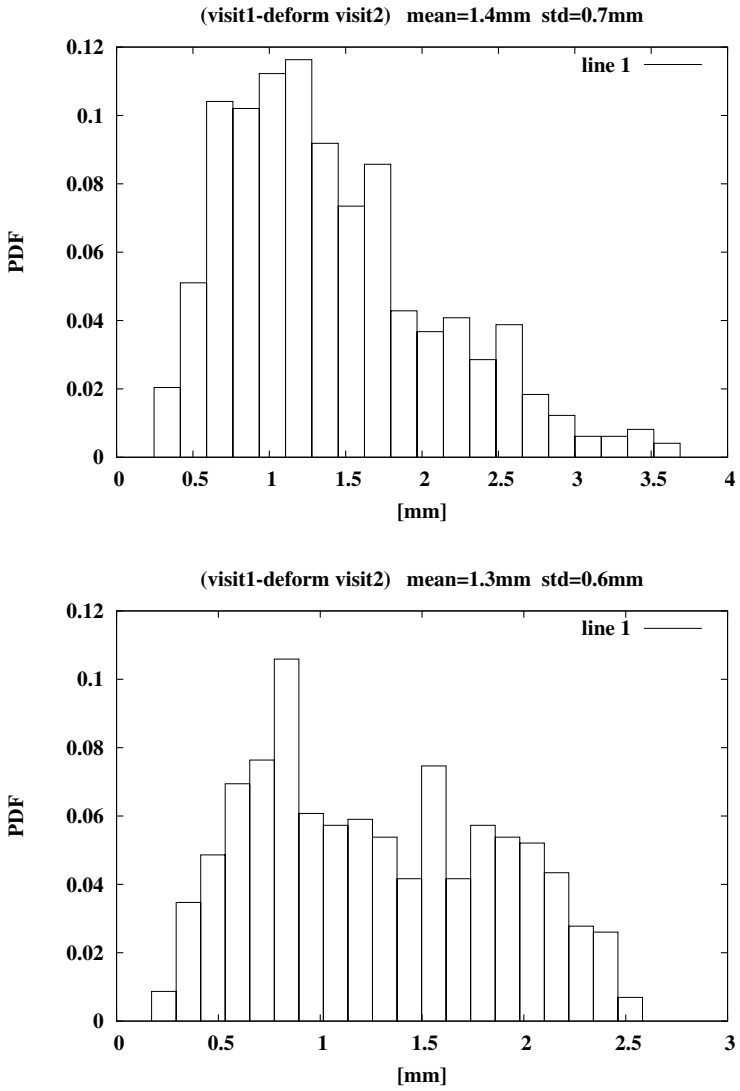

Figure 3.20: Left and middle portal vein results: mean and standard deviation of the distances between the deformed surface from visit 1 and the original data from visit 2.

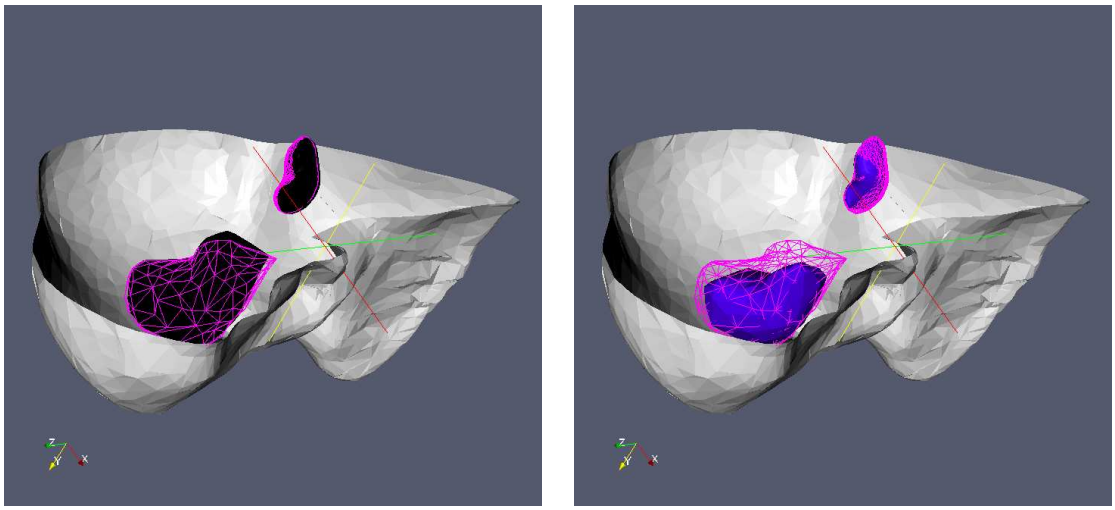

Figure 3.21: Deformation results for both left portal vein and tumor: Left) in black the results of rigid-ICP and in pink the modeling results of deform-ICP and FEM. Right) in blue the actual positions from visit 2 ans in pink the modeling results of deform-ICP and FEM.

the tumor position identified on the CT scan adapt and adjust to the new position of the patient at the time of treatment. Figure 3.22 shows the accuracy of tumor deformation determined by visual comparison of the predicted and actual contour positions.

The tumor phantom model that we developed using plastic beads and a bovine liver is simple, inexpensive and effective. This model may be useful for future algorithm development, for teaching and for continuing medical education.

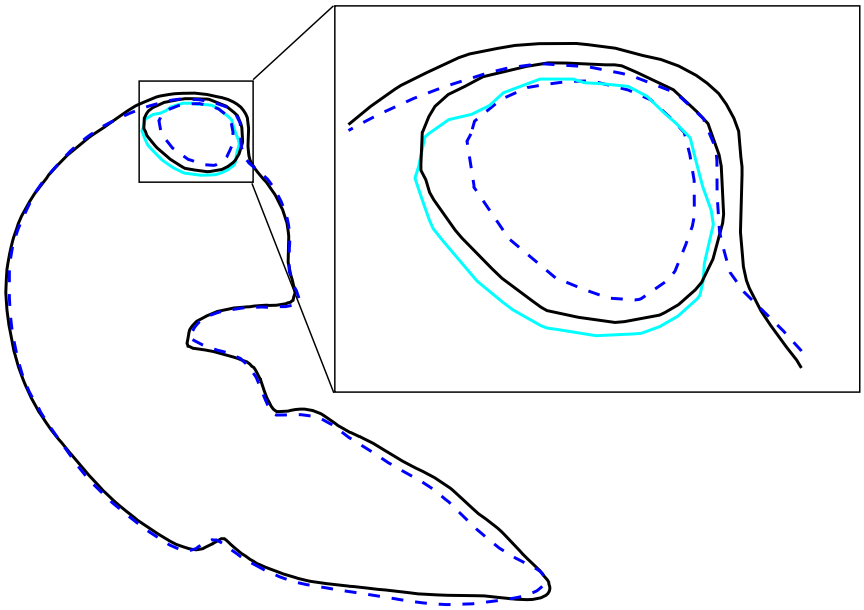

Figure 3.22: Cross-section FEM deformation result : dark solid lines represents the pre-treatment, dotted lines represents post-treatment, and light gray (blue) the deformed pre-treatment tumor.

Chapter 4

Conclusions

Two image-based monitoring approaches were combined and evaluated for their capacity to characterize and track changes in shape and positions of organs during treatment were evaluated. Image registration describes the process of establishing spatial correspondence between features in a dynamic or temporal sequence of images, in order to obtain improved diagnostic discrimination and for therapy or surgical planning. For rigid registration, feature alignment is described as differences in global positioning. Qualitative assessment of shapes can characterize changes in 3-D images across consecutive studies thereby providing an objective means for assessing stages of disease progression and response to treatment. In non-rigid registration, the transformation can accommodate deformations due to surgical intervention, soft tissue properties, temporal changes in tumor growth or due to radiotherapy treatment. In the context of surgical interventions or therapy planning realistic deformable registration models are essential for any approach to be accurate and reliable. Advanced clinical applications have become a critical component of the work flow of radiologists as well as the team of other clinicians who interact with the image data sets. Our vision was to leverage our core expertise in detection and registration to deliver applications that directly meet these clinical needs for various care areas.

References

[1] V.W. Swayze, N.C. Andreasen, R.J. Alliger, J.C. Ehrhardt, W.T. Yuh," Structural brain abnormalities in bipolar affective disorder. Ventricular enlargement and focal signal hyperintensities" , Archives of General Psychiatry, Vol.47(11), 1054-1059, 1990.

[2] G.S. Figiel, K.R.Krishnan, V.P. Rao et al," Sub-cortical hyper intensities on brain magnetic resonance imaging: a comparison of normal and bipolar subjects", Journal of Neuropsychiatry & Clinical Neurosciences , Vol. 3(1), 18-22, 1991.

[3] F.R. Volkmar, A. Klin,"Asperger's Syndrome: guidelines for assessment, diagnosis,treatment and intervention" Learning Disabilities Association of America, 1995.

[4] M.V. Durand, D.H. Barlow, "Abnormal Psychology: An Introduction", Wadsworth Thomson Learning, 2nd Edition, 173-205, 2000.

[5] A.L. Smith and MM.Weissman, Epidemiology. In: Paykel ES, ed. Handbook of affective disorders. Edinburgh: Churchill Livingstone: 111-129, 1992.

[6] S.B. Guze and E. Robins, "Suicide and primary affective disorders", Br J Psychiatry 117:437-438, 1970.

[7] J.M. Llovet, J. Fuster, J. Bruix, "Intention-to-treat analysis of surgical treatment for early hepatocellular carcinoma: resection versus transplantation", Hepatology, vol. 30, pp. 1434-1440, 1999.

[8] G.M. Hargreaves, R. Adam, H. Bismuth, "Results after nonsurgical local treatment of primary liver malignancies" Langenbecks Arch Surg, vol. 385, 185-193, 2000.

[9] S.N. Goldberg, D.E. Dupuy, "Image-guided radiofrequency tumor ablation: challenges and opportunities" - part I and II, J. Vasc Intervent Radiol, vol. 12, 1021-1032, 1135-1148, 2001.

[10] S.N. Goldberg, G.S. Gazelle, P.R. Mueller, "Thermal ablation therapy for focal malignancy: a unified approach to underlying principles, techniques, and diagnostic imaging guidance", Am. J. Radiology, vol. 174, 323-331, 2000.

[11] S. Rossi E. Buscarini, F. Garbagnati, "Percutaneous treatment of small hepatic tumors by an expandable RF needle electrode" Am. J Roentgenol, vol.170, 1015-1022, 1998.

[12] S. A. Curley, F. Izzo, P. Delrio, "Radiofrequency ablation of unresectable primary and metastatic hepatic malignancies: results in 123 patients, Ann Surgical , vol.230, 1-8, 1999.

[13] L. Buscarini, E. Buscarini, M. Di Stasi et al, "Percutaneous radiofrequency ablation of small hepatocellular carcinoma: long term results" , European Radiology, vol.11, 914-921, 2001.

[14] R. Lencioni, D. Cioni, L. Crocetti, et al., "Early-stage hepatocellular carcinoma in patients with cirrhosis : long-term results of percutaneous image-guided radiofrequency ablation", Radiology, vol. 234, 961-967, 2005.

[15] D.S. Lu, N. C. Yu, S.S. Raman et al, " Radiofrequency ablation of hepatocellular carcinoma: treatment success as defined by histologic examination of the ex planted liver", Radiology, vol. 234. 954-960, 2005.

[16] S. N. Goldberg, C. J. Grassi, J. F. Cardella et al, " Image-guided tumor ablation: standardization of terminology and reporting criteria" for the Society of Interventional Radiology Technology Assessment Committee and the International Working Group on Image-Guided Tumor Ablation." J. Vasc. Interv. Radiol., vol. 16, pp. 765-778, 2005.

[17] S. Loncaric, "A survey of Shape analysis techniques", Pattern Recognition, Vol 31(8), 983-1001, 1998.

[18] T.Pavlidis, "A review of algorithms for shape analysis", Computer Graphics and Image Processing, Vol. 7, 68-88, 1984.

[19] H. Freeman, "On the encoding of arbitrary geometric configurations", IRE Trans. on Electron. Comput., EC-10, 260-268, 1961

[20] H. Freeman," Computer processing of line-drawing images", Computing Surveys, Vol.6, 57-97, 1974.

[21] R. Klette, "The m-dimensional grid point space", Computer Vision Graphics and Image Processing, Vol. 30, 1-12, 1985.

[22] I. Stojmenovic and R. Tosic, "Digitization schemes and the recognition of digital straight lines, hyperplanes and flats in arbitrary dimensions", Contemporane Mathematics, Vol.119, 197-212, 1991.

[23] T. Kaneko and M. Okudaira. "Encoding of arbitrary curves based on the chain code representation". IEEE Trans. on Communications, Vol. COM-33, No. 7, 697–707, 1985.

[24] O. Baruch and M.H. Loew. "Segmentation of two-dimensional boundaries using the chain code", Pattern Recognition, Vol. 21, No. 6 581–589, 1988.

[25] F. Marqués, J. Sauleda, and A. Gasull. "Shape and location coding for contour images", Proc. of the 1993 Picture Coding Symposium, p. 18.6, Lausanne, Switzerland, 17-19, 1993.

[26] E. Brisbiesca, "A chain code for representing 3D curves", Pattern Recognition, Vol. 33, 755-765, 2000.

[27] C. Zahn and R. Roskies, "Fourier descriptors for plane closed curves", Computer Graphics and Image Processing, Vol. 21, 269 -281, 1972.

[28] E. M. Arkin, L. P. Chew, D. P. Huttenlocher et. al, “An efficient computable metric for comparing polygonal shapes”, IEEE Transactions on PAMI, Vol. 13, 209-216,1986

[29] G.H. Granlund, "Fourier pre processing for hand print character recognition", IEEE Transactions on Computers, Vol. 21, 195-2 01, 1972.

[30] C.W. Richards and H. Hermani, "Identificat ion of three-dimensional objects using fourier descriptors of the boundary curve ", IEEE Transactions on SMC, Vol. 4, 371-378, 1974.

[31] E. Persoon and K. Fu, "Shape discrimination using fourier descriptors", IEEE Transactions on SMC, Vol. 7, 170-179, 1977.

[32] T.P. Wallace and P. Wintz, "An efficient three-dimensional aircraft recognition algorithm using normalized Fourier descriptors", Computer Graphics and Image Processing, Vol.13, 99-126, 1980.

[33] F. P. Kuhl and C.R. Giardina, "Elliptic Fourier features of a closed contour", Computer Graphics and Image Processing, Vol .18, 236-258, 1982

[34] P. J. Besl and N.D. McKey, “A method for registration of 3D shapes”, IEEE Trans on PAMI, Vol.14(2), 239-256,1992.

[35] B.K.P. Horn, “Closed-form solution of absolute orientation using unit quaternions”, Journal of the Optical Society of Am, Vol.4(4), 629-642,1987.

[36] V.F. Ferrario, C Sforza, et al, “ Shape of the human corpus callosum in childhood”, Investigative Radiology, Vol. 31 (1), 1-5, 1996.

[37] E. L. Lehmann and H. J. D’Abrera, “Nonparametrics: Statistical Methods Based on Ranks”, Englewood Cliffs, NJ: Prentice-Hall, pp. 292, 300, and 323, 1998.

[38] J. B. Antoine Maintz and Max A. Viergever, "A survey of medical image registration", Medical Image Analysis, vol. 2, pp. 1-29, 1998.

[39] H. Lester and S. Arridge, "A survey of hierarchical non-linear medical image registration",Patern Recognition, vol. 32(1), pp. 129-149, 1999.

[40] M. Audette, F. Ferrie and T. Peters, " An algorithmic overview of surface registration techniques for medical imaging", Medical Image Analysis, vol. 4, pp. 201-217, 2000.

[41] D. L. G. Hill, P. G. Batchelor, M. Holden, and D. J. Hawkes, "Medical image registration", Physics in Medicine and Biology, vol. 46, pp.R1-R45, 2001.

[42] D. Rueckert, " Medical Image Registration, chapter 13 Non-rigid registration: Techniques and applications ", pp. 281-303, CRC Press, 2001.

[43] B. Zitova and J. Flusser, "Image registration methods: a survey" , Image and Vision Computing, vol. 21, pp.977-1000, 2003.

[44] W. R. Crum, T. Hartkens, and D. L. G. Hill, "Non-rigid image registration: theory and practice", The British Journal of Radiology, vol. 77, pp. 140-153, 2004.

[45] D. Terzopoulos, J. Platt, A. Barr, K. Fleischer, "Elastically deformable models", Computer Graphics (SIGGRAPH'87), vol. 21, no. 4, pp. 205-214, 1987.

[46] R. Bacjsy and S. Kovacic, " Multiresolution elastic matching", Computer Vision, Graphics and Image Processing, vol. 46, pp.1-21, 1989.

[47] C. Broit, "Optimal Registration of Deformed Images", Ph.D. thesis, Computer and Information Science, University of Pennsylvania. 1981.

[48] K. Roth, "Elastic Registration of Multimodal Medical Images : a Survey", Auszug aus: Kunstliche. Intelligenz, vol. 14(3), pp.11-17, 2000.

[49] G. E. Christensen, "Deformable Shape Models for Anatomy", Ph.D. thesis, Sever Institute of Technology, Washington University, 1994.

[50] G. E. Christensen and H. J. Johnson, "Consistent image registration", IEEE Transactions on Medical Imaging, vol. 20(7), pp.568-582, 2001.

[51] M. Bro-Nielsen, " Medical Image Registration and Surgery Simulation", Ph. D. thesis, IMM Technical University of Denmark, 1996.

[52] M. Bro-Nielsen and C. Gramkov, "Fast fluid registration of medical images", Lecture Notes in Computer Science, Springer, Berlin, vol. 1131, pp. 267-276, 1996.

[53] M. Froskey, B. Davis, L. Goyal, S. Chang et. al., " Large deformation three-dimensional image registration in image-guided radiation therapy", Phys. Med. Biol. vol. 50, pp. 5869-5892, 2005.

[54] S. Cotin, H. Delingette and N. Ayache, "Real-time elastic deformations of soft tissues for surgery simulation", IEEE Trans. on Visualization and Computer Graphics, vol. 5(1), pp.62-73, 1999.

[55] S. Cotin, H. Delingette, N. Ayache, "A hybrid elastic model for real-time cutting, deformations, and force feedback for surgery training and simulation", Visual Computer, vol. 16(8), pp.437-452, 2000.

[56] G. Picinbono, H. Delingette, N. Ayache, "Non-linear and anisotropic elastic soft tissue models for medical simulation", IEEE Intl. Conf. on Robotics and Automation, Seoul, Korea, vol.2 , pp.1370-1375, 2001.

[57] G. Picinbono, H. Delingette, N. Ayache, "Non-linear anisotropic elasticity for real-time surgery simulation", Graphical Models, vol. 65(5), pp. 305-321, 2003.

[58] A. Norton, G. Turk, B. Bacon, J. Gerth, and P. Sweeney, "Animation of fracture by physical modeling", The Visual Computer, vol. 7, pp. 210-219, 1991.

[59] A. Luciani, S. Jimenez, J. L. Florens, C. Cadoz, and O. Raoult, "Computational Physics: A Modeler Simulator for Animated Physical Objects", Proc. Eurographics Workshop Animation and Simulation, pp.425-437, Vienna 1991.

[60] C. Nastar and N. Ayache, "Fast Segmentation, Tracking and Analysis of Deformable Objects", IEEE Proc. Int. Conf. Comp. Vision, pp.275-279, 1993.

[61] S. Sclaroff and A. Pentland, "Modal Matching for Correspondence and Recognition", M. I. T. Media Lab. Perceptual Computing Section Tech. Rep. No. 201, 1993.

[62] M. Desbrun and M. P. Gascuel, "Animating Soft Substances with Implicit Surfaces", Computer Graphics (SIGGRAPH), pp. 287-290, 1995.

[63] U. G. Kuehnapfel and B. Neisius, "CAD-based graphical computer simulation in endoscopic surgery", Endoscopic surgery, vol. 1 pp. 181-184, 1993.

[64] P. Meseure and C. Chaillou, "Deformable body simulation with adaptive subdivision and cuttings", Proceedings of the WSCG, pp. 361-370, 1997.

[65] F. L. Bookstein, "Principal warps: thin-plate spline and decomposition of deformations", IEEE Trans. Pattern Analysis and Machine Intelligence, vol. 11, pp.567-585, 1989.

[66] O. C. Zienkewickz and R.L. Taylor, " The Finite Element Method" , McGraw-Hill Book Co. New York, 4th edition, 1989.

[67] D. Terzopoulos and D. Metaxas, "Dynamic 3D Models with Local and Global Deformations: Deformable Superquadrics", IEEE Trans, PAMI, vol. 13 (7), pp. 703-714, 1991.

[68] T. McInerney and D. Terzopoulos, "Deformable Models in Medical Image Analysis: a Survey", Medical Image Analysis, vol. 1(2), pp.91-108, 1996.

[69] T. McInerney and D. Terzopoulos, "A Dynamic Finite Element Surface Model for Segmentation and Tracking in Multidimensional Medical Images with Application to Cardiac 4D Image Analysis", J. Comp.Med. Imag an Graph, vol.19(1), pp.69-83, 1995.

[70] L. Ding, A. Goshtasby, M. Satter, " Volume image registration by template matching", Image and Computer Vision, vol. 19, pp.821-832, 2001.

[71] K. D. Paulsen, M.I. Miga, F. E. Kennedy, P. J. Hoopes et al., "A computational model for tracking subsurface tissue deformation during stereotactic neurosurgery", IEEE Trans. Biomedical Engineering, vol. 46, pp. 213-225, 1999.

[72] M. Ferrant, A. Nabavi, B. Macq, et al.,"Registration of 3-D intraoperative MR images of the brain using a finite-element biomechanical model", IEEE Trans. on Medical Imaging, vol. 20, no.12, pp. 1384-1397, 2001.

[73] A. Hagemann, K. Rohr, H. S. Stiehl, U. Spetzger and J. M. Gilsbach, "Biomechanical modeling of the human head for physically based, nonrigid image registration", IEEE Trans. on Medical imaging, vol. 18, no.10, pp. 875-884, 1999.

[74] O. Clatz, H. Delingette, I. F. Talos, A.J. Golby, R. Kikinis et. al, "Robust nonrigid registration to capture brain shift from intraoperative MRI", IEEE Trans. on Medical Imaging, vol. 24, no. 11, pp. 1417-1427, 2005.

[75] Q. Yu-Neifert, "A tree-dimensional finite element model to predict the applicability of holographic interferometry to breast tumor detection", Ph. D. thesis, University of Akron, 1995.

[76] F. Azar, D. N. Metaxas and M. D. Schnall, " A deformable finite element model of the breast for predicting mechanical deformations under external perturbations", Journal of Academic Radiology, vol.8, pp.965-975, 2001.

[77] C. Tanner, A. Degenhard, J. Schnabel, A. Smith et. al, "A method for the comparison of biomechanical breast models", Proc. of Workshop on Mathematical Methods in Biomedical Image Analysis, pp.11-18, 2001.

[78] A. Bharatha, M. Hirose, N. Hata, S. K. Warfield, M. Ferrant et al.,"Evaluation of three-dimensional finite element-based deformable registration of pre and intra-operative prostate imaging", Medical Physics, vol. 28, pp. 2551-2560, 2001.

[79] A. Mahomed, C. Devatzikos, R. H. Taylor, T. Dohi and R. Kikinis, "A combined statistical and biomechanical model for estimation of itra-operative prostate deformation", Proc. Med. Image Comput Computer-Assisted Intervention (MICCAI), vol. 2489, pp.452-460, 2002.

[80] R. Alterovitz, K. Goldberg, J. Pouliot, I. J. Hsu et al., "Registration of MR prostate images with biomechanical modeling and nonlinear parameter estimation", Medical Physics, vol. 33, no. 2, pp.446-454, 2006.

[81] J. M. Huygue, D. H. van Campen, T. Arts, R. M. Heethaars, "A two-phase finite element model of the diastolic left ventricle", Journal of Biomechanics, vol. 24, pp. 527-538, 1991.

[82] J. Mackerle, "Finite element modeling and simulations in cardiovascular mechanics and cardiology: A bibliography 1993–2004", Computer Methods in Biomechanics & Biomedical Engineering, vol. 8, pp.581-590, 2005.

[83] K. K. Brock, D. L. McShan, R. K. Ten Haken, et al., " Inclusion of organ deformation in dose calculations", Medical Physics, vol. 30, pp. 290-295, 2003.

[84] J. Liang and D. Yan, "Reducing uncertainties in volumetric image based deformable organ registration", Medical Physics, vol. 30, pp. 2116-2122, 2003.

[85] I. Suramo, M. Paivansalo, and V. Myllyla, " Cranio-caudal movements of the liver, pancreas and kidneys in respiration", Acta Radiology, vol. 25, pp.129-131, 1984.

[86] S. Shimizu, H. Shirato, B. Xo, K. Kagei, T. Nishioka et al., "Three-dimensional movement of a liver tumor detected by high-speed magnetic resonance imaging", Radiotherapy Oncology, vol.50, pp.367-370, 1999.

[87] A. P. King, J. M. Blackall, G.P. Penney, and D. J. Hawkes, "Tracking liver motion using 3-D ultrasound and a surface-based statistical shape model", Proc. IEEE Workshop Mathematical Methods in Biomedical Image Analysis, pp.145-152, 2001.

[88] J. M. Blackall, G. P. Penney, A. P. King, A. N. Adam, and D. J. Hawkes, "Tracking alignment of sparce ultrasound with preoperative images of the liver and an interventional plan using models of respiratory motion and deformation", Proc. SPIE Medical Imaging: Visualization, Image-Guided Procedures, and Display, vol. 5367, pp. 218-227, 2004.

[89] J. L. Boes, P. H. Bland, T. E. Weymouth, L. E. Quint, F. L. Bookstein and C. R. Meyer, "Generating a normalized geometric liver model using warping", Investigative Radiology, vol. 29, pp.281-286, 1994.

[90] K. K. Brock, S. J. Hollister, L. A. Dawson, and J. M. Balter, "Technical note: Creating a four-dimensional model of the liver using finite element analysis", Medical Physics, vol. 29, pp.1403-1405, 2002.

[91] K. Brock, M. Sharpe, L. Dawson, S. Kim, and D. Jaffray, "Accuracy of finite element model-based multi-organ deformable image registration", Medical Physics, vol. 32, no. 6, pp. 1647-1659, 2005.

[92] D. M. Cash, M. I. Miga, T. K. Sinha, R. L. Galloway and W. C. Chapman, "Compensating for intraoperative soft-tissue deformations using incomplete surface data and finite elements" IEEETrans. on Medical imaging, vol. 24, no. 11, pp.1471-1491, 2005.

[93] D. Haemmerich, S. Tungjitkusolmun, T. Staelin, et al, "Finite-element analysis of hepatic multiple probe radio-frequency ablation", IEEE. Trans. om Biomedical Engineering, vol. 49, no. 7, 2002.

[94] A. Charnoz, V. Agnus, and L. Soler, "Portal vein registration for the follow-up of hepatic tumors", Medical Image Computing and Computer-Assisted Interventions (MICCAI), Lecture notes in Computer Science, vol. 3216, pp. 878-886, 2004.

[95] A. Carrillo, J. L. Duerk, J. S. Lewin, and D. L. Wilson, "Semiautomatic 3-D Image registration as applied to interventional MRI liver cancer treatment", IEEE Trans. on Medical Imaging, vol. 19, no. 3, pp. 175-185, 2000.

[96] F. Mokhtarian and A. K. Macworth, "A theory of multiscale, curvature-based shape representation for planar curves", IEEE Trans. on Pattern Analysis and Machine Intelligence, vol.14., no.8, pp. 789-805, 1992.

[97] A. Rangarajan, H. Chui, E. Mjolsness, S. Pappu, L. Davachi, P. Goldman-Rakic and J. Duncan, ¨A robust point matching algorithm for autoradiograph alignment¨, Medical Image Analysis , vol. 4(1), pp:379-398, 1997.

[98] S. Gold, A. Rangarajan, C. P. Lu, S. Pappu, and E. Mjolsness, ¨New algorithms for 2-D and 3-D point matching: pose estimation and correspondence¨, Pattern Recognition, vol. 31(8), pp. 1019-1031, 1998.

[99] H. Chui, J. Rambo, J. Duncan, R. Schultz, A. Rangarajan, ¨Registration of cortical anatomical structures via robust 3D point matching¨, Information Processing in Medical Imaging (IPMI), Springer, pp. 168-181, 1999.

[100] H. Chui and A. Rangarajan, ¨A new point matching algorithm for non-rigid registration¨, Computer Vision and Image Understanding, vol. 89(2-3), pp. 114-141, 2003.

[101] D. Geiger and F. Girosi, "Parallel and deterministic algorithms from MRFs: Surface reconstruction", IEEE Trans. Pattern Analysis and Machine Intelligence, vol. 13, no. 5, pp. 401-412, 1991.

[102] D. L. Logan, "A First Course in the Finite Element Method", PWS Publishing Company, 1st edition, 1986.

[103] http://mipav.cit.nih.gov.

[104] W. E. Lorensen and H.E. Cline, "Marching Cubes: A High Resolution 3D Surface Reconstruction Algorithm ", ACM Computer Graphics, vol. 2, no. 4, pp. 163-169, July 1987.

[105] http://www.vtk.org.

[106] G. Taubin, T. Zhang and G. Golub, "Optimal Surface Smoothing as Filter Design", Proceedings of the 4th European Conference on Computer Vision, Lecture notes in Computer Science, vol. 1064-I, pp. 283 - 292, 1996.

[107] M. Garland and P. S. Heckbert, "Surface Simplification Using Quadric Error Metrics", Proc. of the 24th Conference on Computer Graphics and Interactive Techniques (SIGGRAPH), pp. 209-216, 1997.

[108] http://tetgen.berlios.de

[109] H. Si and K. Gartner, “Meshing Piecewise Linear Complexes by Constrained Delaunay Tetrahedralizations”, Proc. of the 14th International Meshing Round table, September 2005.

[110] http://www.z88.org.

[111] Y. C. Fung, "Biomechanics: Mechanical properties of living tissues", Springer, New York, 1993.

[112] http://autotrace.sourceforge.net

[113] J. R. Shewchuk “Delaunay Refinement Algorithms for Triangular Mesh Generation”, Computational Geometry: Theory and Applications vol. 22 no. (1-3), pp. 21-74, May 2002.

[114] J. R. Shewchuk, “Triangle: Engineering a 2D Quality Mesh Generator and Delaunay Triangulator”, Applied Computational Geometry: Towards Geometric Engineering “(Ming C. Lin and Dinesh Manocha, editors), of Lecture Notes in Computer Science, vol.1148, pp. 203-222, Berlin, May, 1996.

[115] K. Kitamura, H. Shirato, S. Shimizu, et al.,"Registration accuracy and possible migration of internal fiducial gold marker implanted in prostate and liver treated with real-time tumor-tracking radiation therapy (RTRT)", Radiotherapy and Oncology, vol.62, no. 3, pp.275-281, 2002.

[116] K. Kitamura, H. Shirato, Y. Seppenwoolde, et al., "Tumor location, cirrhosis, and surgical history contribute to tumor movement in the liver, as measured during stereotactic irradiation using a real-time tumor-tracking radiotherapy system", Int. Journal of Radiat. Oncol Biol Phys, vol. 56, pp. 221-228, 2003.

Curriculum Vita

Gabriela Niculescu

1988	Graduated from "Gheorghe Munteanu-Murgoci" Theoretic High School, Braila, Romania.
1989 - 1994	Attended "University Politehnica of Bucharest, Romania.
1994	B. S. in Bioengineering, University Politehnica of Bucharest, Romania.
1995 - 1998	Computer programmer, Ubi Soft, Romania.
1999 - 2003	M. S. Graduate student in Biomedical Engineering, Rutgers, The State University of New Jersey.
1999 - 2000	Research Assistant in Department of Psycology, Rutgers, The State University of New Jersey.
2000 - 2003	Research Assistant in Center for Biomedical Imaging and Informatics, University of Medicine and Dentristy of New Jersey.
October, 2003	M.S. in Biomedical Engineering, Rutgers, The State University of New Jersey.
2003 - 2008	Ph.D. Graduate student in Joint program Biomedical Engineering, Rutgers, The State University of New Jersey and Biomedical Sciences, University of Medicine and Dentristy of New Jersey.
2003 - 2008	Research Assistant in Center for Biomedical Imaging and Informatics, University of Medicine and Dentristy of New Jersey.
May, 2008	Ph.D. in Joint program Biomedical Engineering, Rutgers, The State University of New Jersey and Biomedical Sciences, University of Medicine and Dentristy of New Jersey.